

Measurements of the Quasi-Elastic and Elastic Deuteron Tensor Asymmetries

A Proposal to Jefferson Lab PAC 44
(Update to PR12-15-005 and LOI12-14-002)

E. Long,^{† ‡} K. Slifer,[†] P. Solvignon,[†] T. Badman, L. Hammed, M. Holtrop, N. Lajoie, S. Li, K. McCarty, R. Paremuzyan, D. Ruth, S. Santiesteban, B. Yale, R. Zielinski
University of New Hampshire, Durham, NH 03824

D. Day,[†] D. Keller,[†] D. Crabb, S. Liuti, O. A. Rondon, V. Sulkosky, J. Zhang
University of Virginia, Charlottesville, VA 22903

D. Higinbotham[†], J. Beričič, A. Camsonne, J. P. Chen, S. Covrig Dusa, D. Gaskell, C. Keith, P. Nadel-Turonski, K. J. Park, G. Smith, S. Wood
Thomas Jefferson National Accelerator Facility, Newport News, VA 23606

K. Anoil
California State University - Los Angeles, Los Angeles, CA 90032

Z. Ye
Duke University, Durham, NC 27708

W. U. Boeglin, M. Sargsian, P. Markowitz
Florida International University, Miami, FL 33199

W. Cosyn
Ghent University, 9000 Ghent, Belgium

B. Dongwi, N. Kalantarians, M. Kohl, A. Liyanage, J. Nazeer
Hampton University, Hampton, VA 23668

T. Breclj, S. Širca, S. Štajner
Jožef Stefan Institute and University of Ljubljana, Slovenia

B. Bertozzi, S. Gilad
Massachusetts institute of Technology, Cambridge, MA 02139

K. Adhikari
Mississippi State University, Mississippi State, MS 39762

[†]Spokesperson

[‡]Contact: ellie@jlab.org

A. Ahmidouch, S. Danagoulian
North Carolina A&T State University, Greensboro, NC 27411

W. Tireman
Northern Michigan University, Marquette, MI 49855

M. Strikman
Pennsylvania State University, University Park, PA 16802

R. Gilman
Rutgers University, Piscataway, NJ 08854

M. Elaasar
Southern University and New Orleans, New Orleans, LA 70126

W. van Oers
University of Manitoba, Winnipeg, MB, Canada

G. A. Miller
University of Washington, Seattle, WA 98195

D. Androic
University of Zagreb, HR-10000 Zagreb, Bijenicka 32, Croatia

Abstract

In this update to PR12-15-005 and LOI12-14-002, we propose the first measurement of the tensor asymmetry A_{zz} in the quasi-elastic region through the tensor polarized $D(e, e')X$ channel; an asymmetry that is sensitive to the nucleon-nucleon potential at short distances. Previous measurements of A_{zz} have been used to extract b_1 in the DIS region and T_{20} in the elastic region. A unique feature of the measurements proposed here is that they select compact deuteron configurations both through the tensor asymmetry, which enhances the D-state, and the choice of $x > 1$ kinematics. Taken together, these features amplify short-range effects.

In the quasi-elastic region, A_{zz} will be used to describe the nature of the short-range repulsion and the tensor force strength, which is related to the deuteron D-state probability. It has been shown that scattering from a tensor polarized deuteron can be used to discriminate among different nuclear force potential models [1], especially with respect to the short-range behavior and tensor force strength. The nuclear models predict that the S and D-state components are strongly dependent on momentum and are sensitive to the repulsive core of the NN interaction at short distances [2]. From D-state enhancement, A_{zz} is sensitive to the choice of hard or soft NN potentials in the high $x > 1.4$ region. Until now, there has been no unambiguous experimental evidence for which is more valid. A_{zz} is also sensitive to relativistic effects at much lower momenta than in the unpolarized case, causing light cone and virtual nucleon models to begin diverging at $x \approx 1.2$. By measuring A_{zz} over a large range in x , we can experimentally probe tensor effects that are important for understanding short range correlations in nuclei.

The kinematic requirements of A_{zz} allow for the simultaneous measurement of elastic T_{20} at multiple Q^2 points ranging from $0.2 < Q^2 < 1.8 \text{ GeV}^2$, the largest range ever for a single T_{20} experiment. At low $Q^2 \sim 0.2 \text{ GeV}^2$, T_{20} is well known experimentally and theoretically, making it an ideal calibration point for the tensor polarized target. We will measure T_{20} at a Q^2 where previous results systematically disagree, as well as provide a crucial check of the only existing data at large Q^2 .

The possibility to measure tensor observables with high precision at Jefferson Lab has attracted the attention of a number of theorists, which have provided a range of predictions that require a measurement of A_{zz} to constrain. In the words of both the PAC42 and PAC43 theory reviews, “The measurement proposed here arises from a well-developed context, presents a clear objective, and enjoys strong theory support. It would further explore the nature of short-range pn correlations in nuclei, the discovery of which has been one of the most important results of the JLab 6 GeV nuclear program.”

We propose an experimental determination of A_{zz} and T_{20} utilizing the same equipment as the E13-12-011 b_1 experiment. Six different Q^2 values of A_{zz} and four of T_{20} will be measured over the course of 34 days, with 11 additional days of overhead. The proposed A_{zz} measurements are more than an order of magnitude less sensitive to systematic uncertainties than E13-12-011 and will measure asymmetries of order 100%, so this experiment could also be utilized to better understand the in-beam conditions and time-dependent systematic effects of a tensor polarized target for the b_1 experiment. This experiment will play a crucial role in the larger tensor program at Jefferson Lab, which continues to generate interest from experimental, polarized target, and theoretical spin communities, by providing the first experimental data in a region where there remains a gap in our understanding of the simplest composite nuclear system.

Foreword

This proposal is an update to both LOI12-14-002 and PR12-15-005, which we note has a history of strong support from both PAC42 and PAC43. Below is a brief outline of the PAC43 C2 conditions and TAC concerns, as well as our current efforts to address them. A more in-depth summary of all PAC comments and responses is included in Sec. 4.

1. PAC43 Conditions

- (a) Provide quantitative comparison between the proposed tensor asymmetry and unpolarized measurements regarding sensitivity to the D-state probability
 - i. In Sec. 1.1.1, we include new calculations for all electron-deuteron observables alongside current measurements, which shows that wavefunctions can only be separated to $\sim 1\%$ and determined to $\sim 1\sigma$ for the unpolarized and vector polarized cases. Tensor polarization allows for a separation of up to $\sim 60\%$ and discrimination of up to $> 4\sigma$ at $x > 1.3$, as shown in Fig. 17 and Sec. 3.4. We also note that different relativistic models can be determined at $> 6\sigma$ at $x < 1.3$.
- (b) Investigate the possibility of negative tensor polarization (P_{zz}) to reduce uncertainties, particularly systematic effects
 - i. Although it is possible to achieve $P_{zz} < 0$ with the DNP target, it can not be maintained at 1 K due to temperature-dependent depolarization as described in Sec. 3.5.3. However, we can minimize systematic uncertainties to $< 10\%$ while using only $P_{zz} > 0$ as described in Sec. 3.4.2. We also plan to flip the initial vector polarization during each cycle to remove systematic effects while maintaining $P_{zz} > 0$ as shown in Fig. 22 and Sec. 3.5.4.
- (c) The method of NMR line shape analysis to measure tensor polarization needs to be further developed
 - i. Progress has been made in determining and increasing P_{zz} from line shape analysis, which includes a publication in Eur.J.Phys. A. that is currently under review. By developing this technique, not only are we able to more accurately measure P_{zz} , but a refined version of RF hole-burning has been developed as described in Sec. 3.5.3. Results on butanol that have achieved $P_{zz} > 30\%$ are in Fig. 20.

2. PAC43 TAC Concerns

- (a) Tensor enhancement by RF hole burning is in the R&D stage
 - i. As noted above, the R&D effort is on-going and has already made significant improvements. Results described in Sec. 3.5.3 and shown in Fig. 20 have demonstrated $P_{zz} > 30\%$ on butanol. These techniques are now being applied to ND₃, with expected results in the coming months.
- (b) Only one cross-check polarization measurement from T_{20} is planned. Can this check be relied upon at all measurements?

- i. Although we expect the line shape analysis method to be reliable for all measurements, we included an independent measurement of P_{zz} from T_{20} at a single Q^2 point, as described in Sec. 3.5.2. Agreement from this cross-check at any Q^2 will indicate that the line shape analysis method is valid for all P_{zz} measurements.
- (c) Will fringe fields from the SHMS magnets, particularly the Horizontal Bender, cause any issues with the target magnet?
 - i. We expect effects of < 15 ppm on the target as described in Sec. 3.5.6, which is well within the 100pm field uniformity required. We also note similar concerns of magnetic cross-talk during the Hall A g2p experiment, but even during catastrophic septa failure the target field uniformity was maintained at < 100 ppm as shown in Fig. 24.
- (d) In case of effective target density change by ND_3 bead displacement, will the data around the event be usable?
 - i. Discussed in Sec. 3.4.2.4, data recovery would simply involve splitting the data to before and after the event and adding an extra run to measure the new target length.
- (e) 75 nA is the nominal lower limit of existing readout systems in Hall C
 - i. We plan on running above this limit at 80-100 nA and provided conservative statistics. On the first day we will optimize beam current and target depolarization. A demonstration of 90 nA statistics was shown in LOI12-14-002. As noted in Sec. 3.3, previous experiments that have run at similar currents include SANE (E07-003), RSS (E01-006), and GEN (E93-026).

In summary, this proposal represents the recent efforts that will allow us to meet the physics goals of this experiment. We have developed methods to maintain systematic uncertainties to $< 10\%$ even with utilizing only positive tensor polarization, allowing us to determine between relativistic calculation methods to $> 6\sigma$ and to distinguish between hard and soft wavefunction inputs up to $> 4\sigma$, both of which we've shown are currently impossible using either an unpolarized or vector polarized target. Target development is on-going, and recent studies on deuterated butanol over this past year have produced $> 30\%$ tensor polarization, with plans to transfer these techniques to ND_3 in the very near future. We also note that the authors listed on this proposal reflect the available expertise in both theoretical and experimental techniques that, in the words of the theory reviews from both PAC42 and 43, will allow us to “further explore the nature of pn correlations in nuclei, the discovery of which has been one of the most important results of the JLab 6 GeV program.”

Contents

1	A_{zz} Motivation	8
1.1	Probing the Deuteron Wavefunction	9
1.1.1	The Need for Tensor Polarization	11
1.2	Study of the Relativistic NN Bound System	13
1.3	Final State Interactions	16
1.4	Interest from Theorists	16
2	T_{20} Motivation	18
3	The Proposed Experiment	20
3.1	A_{zz} Experimental Method	20
3.2	T_{20} Experimental Method	22
3.3	Kinematics	23
3.4	Uncertainty Estimates	25
3.4.1	Statistical Uncertainty	29
3.4.2	Systematic Uncertainty	31
3.4.2.1	Time Dependent Factors	33
3.4.2.2	Drift Mitigation	35
3.4.2.3	Trigger-Tracking	36
3.4.2.4	Target Dilution and Length	36
3.4.2.5	Solid Angle	38
3.4.2.6	Beam Current Monitors	38
3.4.2.7	Systematic Summary	39
3.5	Polarized Target	39
3.5.1	Polarization Analysis	41
3.5.2	Elastic Normalization of Tensor Polarization	41
3.5.3	Tensor Polarization Enhancement	42
3.5.4	Depolarizing the Target	43
3.5.5	Dilution Factor	44
3.5.6	Target and Horizontal Bender Magnets	45
3.6	Overhead	46
4	Previous PAC Comments and Concerns	46
4.1	PAC42 Theory Advisory Committee	46
4.2	PAC43 Theory Advisory Committee	47
4.3	PAC42 Technical Advisory Committee	48
4.4	PAC43 Technical Advisory Committee	49
4.5	PAC42 Program Advisory Committee	50
4.6	PAC43 Program Advisory Committee	50
4.7	Response to PAC42 Concerns	51

4.8 Response to PAC43 Concerns	52
5 Summary	53

1 A_{zz} Motivation

The deuteron is the simplest composite nuclear system, and in many ways it is as important to understanding bound states in QCD as the hydrogen atom was to understanding bound systems in QED. However, our experimental and theoretical understanding of the deuteron at short distances remains unsatisfactory. A well-constrained theoretical description is essential for understanding the dynamics of short-range NN correlations in nuclei, which are dominated by tensor interactions up to 700 MeV/ c internal momenta.

It has been known for many years that in addition to the $L = 0$ (S-state) component of the ground state of the deuteron, there is also present at the 4 – 7% percent level, an $L = 2$ (D-state) component. In 1939, Schwinger pointed out that the quadrupole moment of the deuteron provided irrefutable evidence for a tensor component of the nuclear force. The tensor force doesn't conserve either the spin (S) or the orbital angular momentum (L), but only the total angular momentum (J), therefore allowing mixing between the predominant spherically symmetric S state and configurations with the $L = 2$ D-state.

Tensor polarization enhances the D-state contribution, which compresses the deuteron [2], making the system more sensitive to short-range effects. Understanding the short distance nucleon-nucleon potential of the deuteron is essential for understanding short-range correlations, as they are largely dependent on the tensor force [3]. Both inclusive and exclusive electron scattering at $x > 1$ have revealed the strength of short range correlations and their isospin dependence at large momenta ($p > k_f$) [4], which is well supported by theory [5]. We can resolve the short-range structure of nuclei on the level of nucleon and hadronic constituents by utilizing processes that transfer both energy and momentum larger than the scale of the NN short-range correlations to the nucleon constituents, particularly at $Q^2 > 1$ (GeV/ c)².

By taking a ratio of cross sections from electron scattering from tensor-polarized and unpolarized deuterons,

$$A_{zz} = \frac{2}{fP_{zz}} \left(\frac{\sigma_p}{\sigma_u} - 1 \right), \quad (1)$$

the S and D-wave states can be disentangled, leading to a fuller understanding of the attractive and repulsive components of the nucleon core. A measurement of A_{zz} is sensitive to the ratio $\frac{D^2 - SD}{S^2 + D^2}$ and its evolution with increasing minimal momentum of the struck nucleon.

Within the past few years, there has been a strong theoretical effort to better understand the deuteron through the quasi-elastic A_{zz} observable. First calculated in 1970's to demonstrate its usefulness in probing the short-range nuclear core in the region where the D-state dominates [6], it has recently been revisited by M. Sargsian and M. Strikman who have calculated A_{zz} in the $x > 1$ range using relativistic light-cone and virtual-nucleon methods [7]. For quasi-elastic A_{zz} , these methods differ by up to a factor of two and can be discriminated experimentally at the $> 6\sigma$ level. Probing these relativistic models is crucial for advancing our understanding of short range correlations, which are dominated by tensor interactions [4]. Additionally, the calculations are sensitive to the S/D ratio of the input deuteron wave functions at large relative momenta $k > 300$ MeV, which show a large discrepancy at high x and can be used to further the original intent of A_{zz} to discriminate between soft and hard pn potentials at $> 4\sigma$.

A number of other theoretical efforts have begun to further use A_{zz} to understand the simplest composite nuclear system. Effects from final state interactions have been calculated using a virtual nucleon model with various NN potentials by W. Cosyn, and are expected to have a significant effect on A_{zz} at large x and must be understood to probe nucleonic effects. Calculations that emphasize the importance of this experiment to determine between relativistic deuteron wavefunction treatments have been provided by G.A. Miller. For every kinematic setting, H. Arenhovel has provided calculations of all $D(e, e')$ observables for the unpolarized, vector, and tensor polarized cases that emphasize why a tensor polarized target is needed to achieve the physics goals of this proposal. His calculations also predict a fall-off of relativistic predictions including meson-exchange and isobar currents that differ greatly from relativistic plane-wave Born approximation at lower Q^2 . Calculations from W. Van Orden are in progress for the low Q^2 region using different nucleon-nucleon potentials, as well as different prescriptions for handling the reaction mechanisms in tensor polarization observables [8]. Although it is difficult to disentangle reaction mechanisms from NN potentials using cross section measurements, previous low Q^2 results have indicated that asymmetries are far less sensitive to the reaction mechanisms [9]. Similar calculations have also been finalized for the $D(e, e')n$ at high Q^2 , high p_m experiment [10].

Measuring A_{zz} in the quasi-elastic region will fill a gap in measurements performed on deuterium scattering. It is directly proportional to the elastic deuteron tensor analyzing powers by $A_{zz} = \sqrt{2} [d_{20}T_{20} + d_{21}T_{21} + d_{22}T_{22}]$. In the deep inelastic region, A_{zz} will soon be measured to extract the tensor structure function b_1 by the relation $A_{zz} \propto \frac{b_1}{F_1^D}$. Not only will measuring A_{zz} in the quasi-elastic region provide information necessary for understanding the fundamental properties of the deuteron, it will be the first experiment to bridge a gap in measurements of electron scattering from tensor-polarized deuterons. We emphasize that this measurement is pushing the limits of understanding the deuteron by going to kinematics where no current measurements exist and where current theoretical understanding remains unsatisfying.

1.1 Probing the Deuteron Wavefunction

It was suggested for some time [11] that to resolve the microscopic structure of nuclei one needs to study scattering at sufficiently large momentum transfer and large relative momenta of the produced nucleons. This logic was confirmed [3] by a series of experiments at SLAC [12] and JLab [13, 14] that directly observed short-range correlations (SRC) in a series of nuclei, as well as JLab measurements that directly probed the deuteron at high p_m [15, 16] and established a similar effect of SRC in the deuteron and in heavier nuclei with pn correlations giving the dominant contribution. Hence, the deuteron serves as a “hydrogen atom” for the studies of the microscopic short-range structure of the nuclei since it is the simplest nuclei that follows SRC scaling.

To achieve further progress, it is necessary to improve our knowledge of the deuteron wave function at high momenta, and to separate the S and D contributions to the high momentum component of the deuteron. The dominance of the D-wave at a large range of the nucleon momenta is expected in a range of the theoretical models, as demonstrated in Fig. 1, but experimentally it was probed in a rather indirect way via measurement of T_{20} for the deuteron form factor [17]. Still, the knowledge of S/D ratio for large momenta is rather poor. Indeed, all wavefunctions are constrained

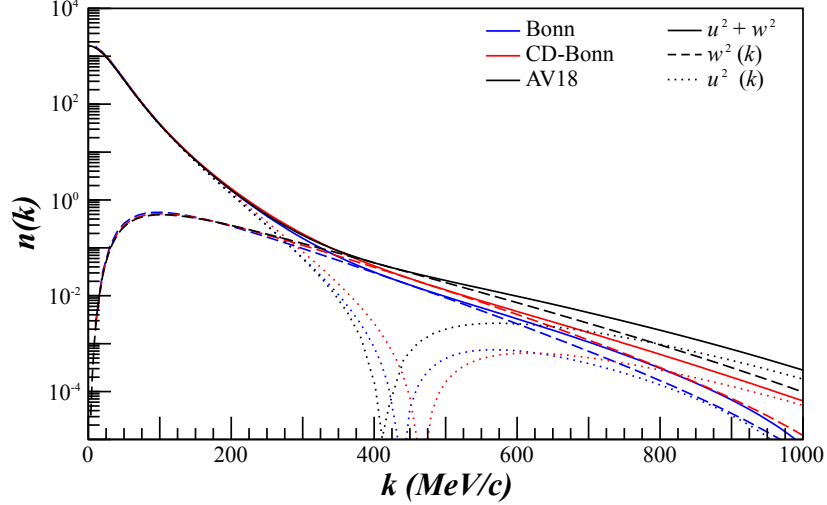


Figure 1: The AV18 [18] (black), Bonn [19] (blue), and CD-Bonn [20] (red) deuteron wavefunctions, showing the dominance of the D-state (dashed) in comparison to the S-state (dotted) in the full wavefunction (solid) at high momentum ($k > 300$ MeV/c).

by low energy data to reproduce the S/D ratio at small momenta while the overall probability of the D-wave in the deuteron differs by a factor up to 1.5, leading to a large difference of the S/D ratio at large momenta. In the impulse approximation, the S and D-states are related to the tensor asymmetry A_{zz} by [6]

$$A_{zz} \propto \frac{\frac{1}{2}w^2(k) - u(k)w(k)\sqrt{2}}{u^2(k) + w^2(k)}, \quad (2)$$

where $u(k)$ is the S-state wave function and $w(k)$ is the D-state wave function.

Ratios of inclusive cross sections at $x > 1$ have demonstrated an early onset of the scaling of the ratios when plotted as a function of the light-cone fraction of the struck nucleon momentum. As a result, the ratios provide a direct measurement of the ratio of the high momentum components in nuclei. Similarly, in the case of scattering from the polarized deuteron we expect the early scaling for the asymmetry when plotted as a function of the minimal struck nucleon momentum or the light cone fraction in the $A(e, e')$ case. It was observed at JLab that the scaling of the ratios begin at $Q^2 \sim 1$ GeV² [13], so covering the range of Q^2 up to 2 GeV² will be sufficient to measure the S/D ratios in an interesting momentum range.

It is worth noting here that in addition to comparing predictions for the different wave functions, one expects to be able to distinguish between non-relativistic and relativistic quantum mechanic models. One of the principal differences between the models is the relation between the spectator momentum and momentum in the wave function. In the non-relativistic model they coincide, while in the light cone model the relation is non-linear starting at $k \sim 250$ MeV/c. This difference is most clearly manifested in the scattering from the polarized deuteron due to a strong dependence of the S/D ratio on the nucleon momentum.

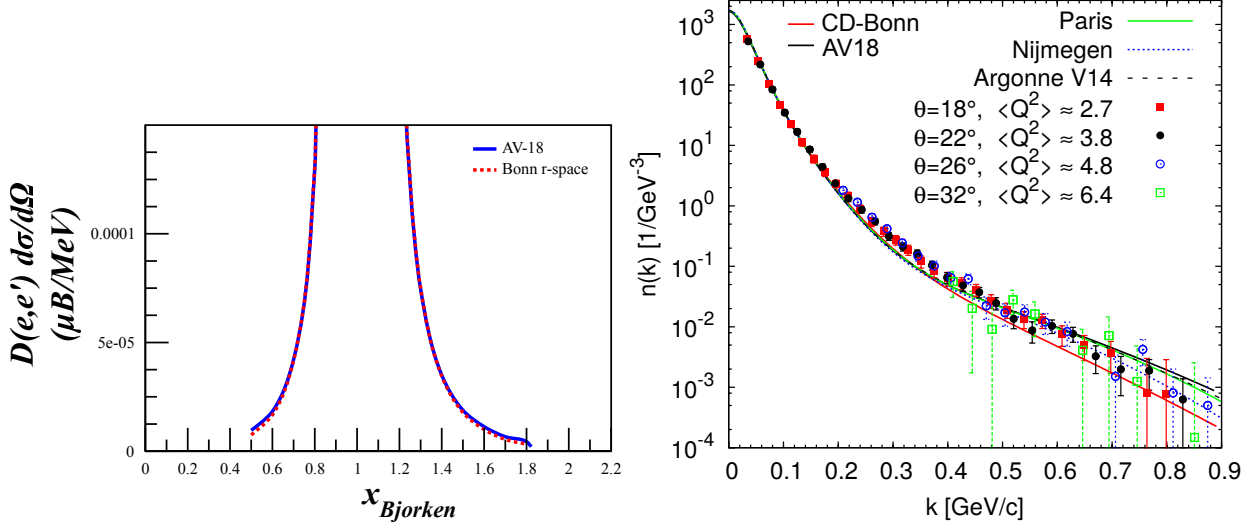


Figure 2: The separation between hard and soft wavefunctions in the case of unpolarized cross sections is extremely difficult to measure, as demonstrated here (left) by calculations provided by H. Arenhovel at our proposed kinematics. Shown alongside (right) are extracted deuteron momentum distributions from recent unpolarized data taken by N. Fomin *et al* [14] emphasize the difficulty in determining between hard and soft wavefunction inputs when using an unpolarized target.

1.1.1 The Need for Tensor Polarization

Asymmetries based on tensor polarization allow for a discrimination between wavefunction inputs that is far greater than in the case for either unpolarized cross-sections or vector polarized asymmetries. Leidmann *et al* describe each of the four vector and tensor polarized asymmetries α_d^V , $\alpha_d^T = A_{zz}/\sqrt{2}$, α_{ed}^V , and α_{ed}^T in [21]. In the case of both a longitudinally and transversely polarized target, $\alpha_d^V = \alpha_{ed}^T = 0$. Calculations using plane-wave Born approximation with relativistic corrections provided by H. Arenhovel at our proposed kinematics show a greatly reduced ability to discriminate between hard and soft wavefunctions in the case of unpolarized cross-sections as shown in Fig. 2. Recent data taken to measure the high-momentum short-range structure of unpolarized nuclei [14] highlights our current best experimental determination between hard and soft wavefunction inputs in the unpolarized case.

Again calculated by Arenhovel, the vector asymmetry α_{ed}^V is more promising in its separation between hard and soft wavefunction inputs, although the difference between them is still small ($\approx 1\%$ absolute asymmetry) as shown in Fig. 3. Current α_{ed}^V measurements [22, 23] have an uncertainty of at best $\pm 1\%$, making it impossible to make a discrimination. Only with a tensor polarized target can we get a large separation ($> 20 - 40\%$ absolute asymmetry) between hard and soft wavefunction inputs, as demonstrated next to the vector asymmetry in Fig. 3. Depending on which models are used, the difference between hard and soft wavefunctions at large x using A_{zz} can be as large as 60% within measureable kinematics.

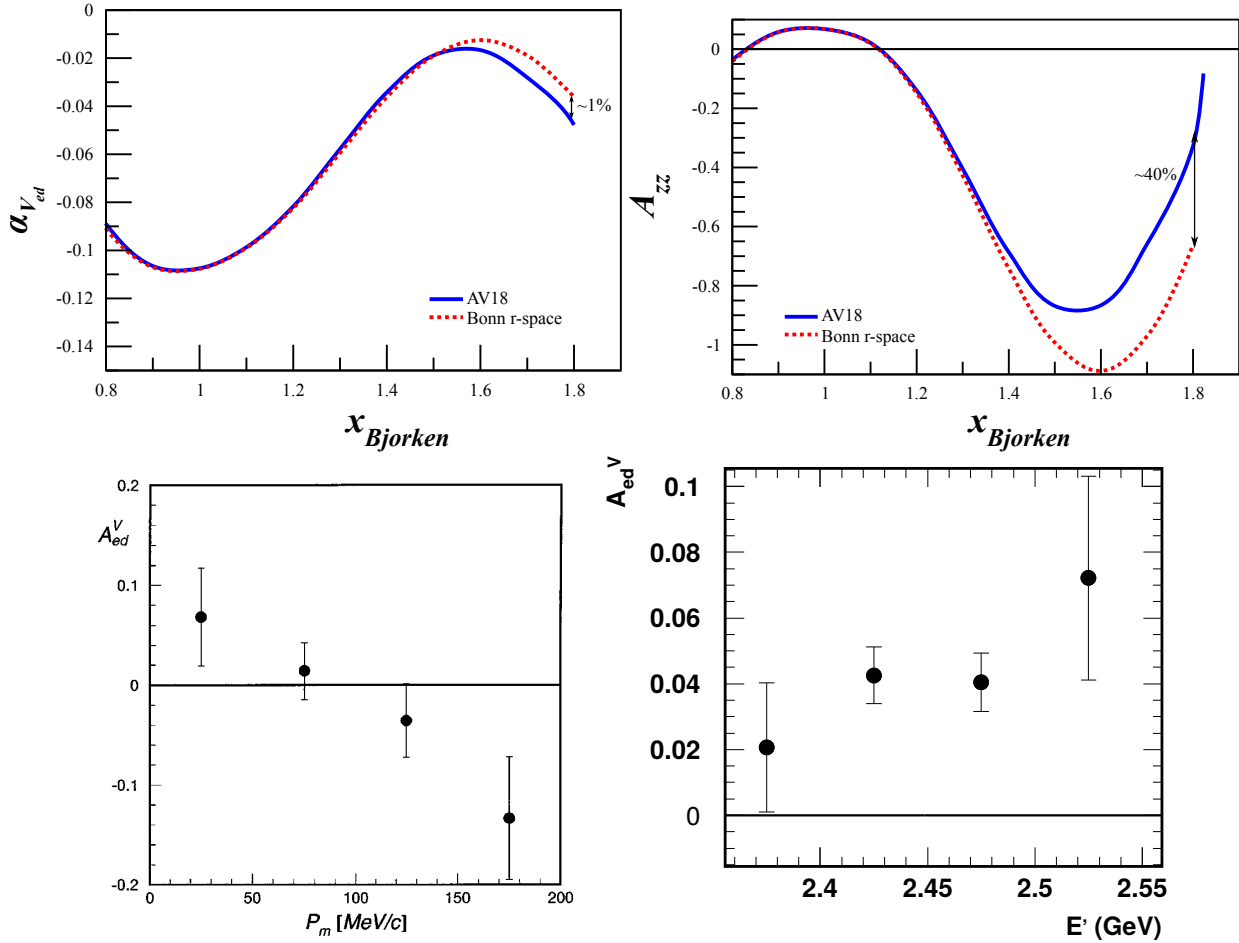


Figure 3: The separation between hard and soft wavefunctions in the case of vector polarized asymmetries (top-left) is also difficult to measure, with a separation of only $\approx 1\%$. This asymmetry was measured during the GEN experiments at Mainz [22] and JLab [23] (bottom) to at best $\pm 1\%$, which would not allow for discriminating wavefunctions. The same is not true for the tensor polarized asymmetry A_{zz} (top-right), which sees a separation of 20 – 40% or higher depending on the model. Calculations shown in the top figures provided by H. Arenhovel.

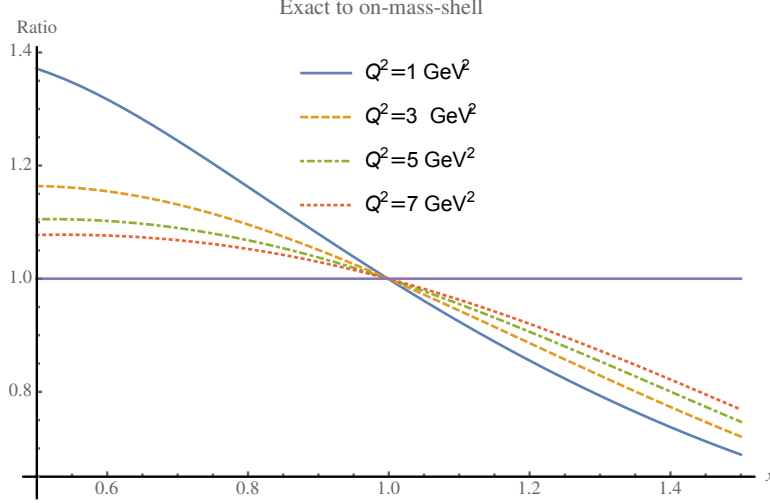


Figure 4: Cross-section ratios of different relativistic treatments indicate that significant errors are seen for values of x that differ from unity, particularly at $Q^2 < 10 \text{ GeV}^2$. Calculations by J. Terry and G. Miller from [28].

1.2 Study of the Relativistic NN Bound System

One of the important issues in studying nuclear structure at short distances is the relativistic description of the bound system. This is an important issue also in understanding the QCD medium effect with recent studies indicating that parton distribution modifications in nuclei are proportional to the high momentum component of nuclear wave function [24].

The deuteron is the simplest bound system and naturally any self-consistent attempt to understand the relativistic effects in the bound nuclear systems should start with the deuteron. The issue of the relativistic description of the deuteron has a long history with extensive research that started in the late 1970's [25, 26, 27, 11]. As noted recently by J. Terry and G. Miller [28], there is a strong need for models of the deuteron wave function that are both realistic and relativistic. This is shown in Fig. 4 where the ratio between exact and on-mass-shell calculations creates a significant uncertainty for values of x differing from unity, particularly for measurements where $Q^2 < 10 \text{ GeV}^2$.

Experimental studies of relativistic effects in the deuteron up to now include the large Q^2 elastic ed scattering [29], however due to complexities in the reaction mechanism [30] the relativistic effects were difficult to isolate. An example from unpolarized data is shown in Fig. 5.

Inclusive $D(e, e')X$ experiments from tensor-polarized deuterons at $Q^2 > 1 \text{ GeV}^2$ and in the $x > 1$ region gives a new possibility to probe the relativistic structure of the deuteron. In this case the use of the tensor polarized deuteron allows us to prepare the nucleus in the most compact state in which, due to the absence of the pure S-wave contribution, the system in average is sensitive to the higher nucleon momenta in the deuteron. At large $Q^2 > 1 \text{ GeV}^2$ kinematics, the probed longitudinal momenta of the bound nucleon is given by $p_z \approx m_N(1 - x)$, or the light cone momentum fraction $\alpha \geq x$. Because of these kinematic conditions and the enhancement of the

D(e,e'), E=20.999 GeV, $\theta=10^\circ$, $Q^2=10 \text{ GeV}^2$

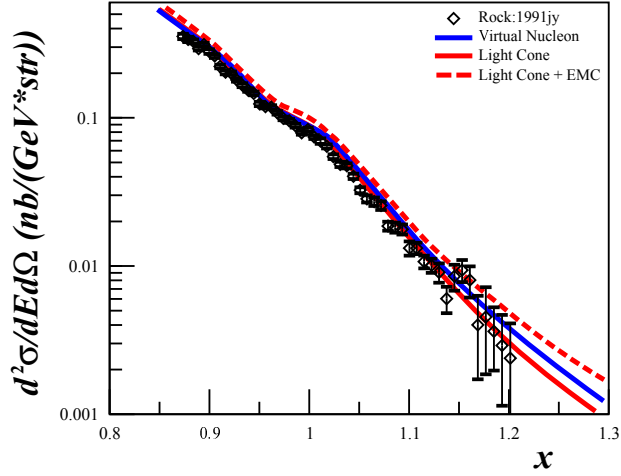


Figure 5: An example of the difficulty in disentangling relativistic light-cone and virtual-nucleon models [7] from unpolarized data [31].

D-wave contribution from tensor polarization, a measurable relativistic effects is expected already at $x \approx 1.2$ as shown in Fig. 6. Such an early onset of the relativistic effects indicates that they can be separated from the choice of NN potentials, which dominate at $x > 1.4$.

The sensitivity to relativistic effects is estimated using the theoretical calculations based on two very different approaches. The first approach treats the virtuality of the bound nucleon within a description of the deuteron in the lab frame by treating the interacting nucleon as being virtual (virtual nucleon, or VN approximation). This is accomplished by taking the residue over the energy of the spectator nucleon. In this case, the deuteron wave function satisfies the covariant equation of the two-nucleon bound system with one spectator being on energy shell [33, 34].

Another approach is based on the observation that high energy processes evolve along the light-cone (LC). Therefore, it is natural to describe the reaction within the light-cone non-covariant framework [11]. Negative energy states do not enter in this case, though one has to take into account so called instantaneous interactions. In the approximation when non-nucleonic degrees of freedom can be neglected, assuming rotational invariance of the LC deuteron wave function around its quantization axis, the relativistic wave function can be related to the nonrelativistic wave function through the introduction of LC pn relative momentum [11, 35],

$$k = \sqrt{\frac{m^2 + p_t^2}{\alpha(2 - \alpha)} - m^2}. \quad (3)$$

In Fig. 6, the prediction for VN [33] and LC [12] approximations are given for the $Q^2 > 1 \text{ (GeV}c)^2$ kinematics proposed. As was previously mentioned, a measurable difference is predicted to be observable already at $x \geq 1.2$. Although J. Terry and G. Miller do not include direct calculations for A_{zz} , in a recent publication they note that this is the only planned experiment to

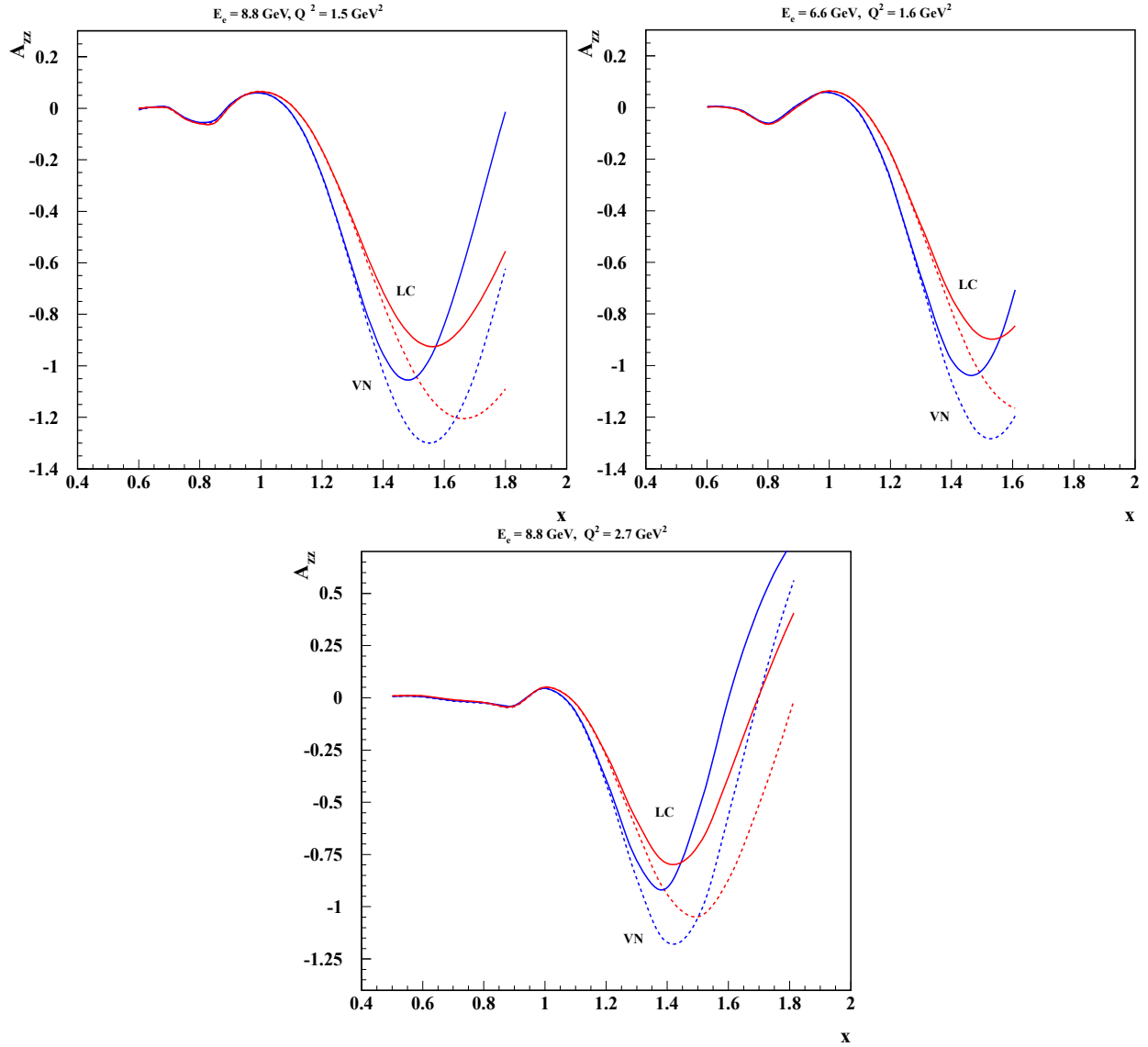


Figure 6: The A_{zz} observable calculated at $Q^2 = 1.5, 1.8, \text{ and } 2.9$ (GeV/c)² using the light-cone (red) and virtual nucleon (blue) models with NN potential inputs of AV18 (solid) and CDBonn (dotted). Calculations provided by M. Sargsian and M. Strikman [7, 32].

specifically test the use of light-cone versus virtual nucleon methods, and make a prediction that the light-front spectator calculations will reproduce the experimental results [28].

1.3 Final State Interactions

In order to accurately determine the nucleonic components of the deuteron’s wave function, it is vital that final state interactions (FSI) are understood. As demonstrated below, FSI can introduce a significant component to A_{zz} , particularly in the large $x > 1.2$ region. Including these effects is necessary for further constraining our theoretical understanding of the deuteron through A_{zz} .

The effects of FSI on A_{zz} have recently been modeled by W. Cosyn in the deep-inelastic region [36] and in the quasi-elastic region discussed in this proposal [37], which is an on-going area of research. Results are shown in Fig. 7-8. The calculations use the virtual nucleon (VN) approximation to compute inclusive observables in electron-induced scattering off the deuteron including the effect of final-state interactions. Amplitudes and observables are computed in an unfactorized manner.

Current calculations include on-shell and off-shell contributions to the FSI amplitudes, but the off-shell contribution is calculated by neglecting any possible singularities of the EM current in the complex plane. Calculations including these are forthcoming. The inclusive observables are computed using the optical theorem in a manner analogous to Ref. [38]. The rescattering of the struck nucleon with the spectator is modeled using an eikonal amplitude. For the calculations included in this proposal, the off-shell contribution to the FSI amplitude has not been suppressed in any manner, such that the maximum possible effect of FSI are estimated.

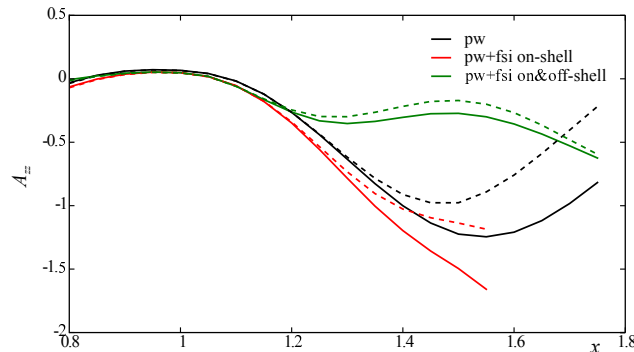


Figure 7: A_{zz} calculation for $E_0 = 8.8 \text{ GeV}^2$ and $Q^2 = 1.5 (\text{GeV}/c)^2$ including contributions from final state interactions. Solid curves were calculated using the CDBonn deuteron wave function, dashed curves using the AV18 deuteron wave function.

1.4 Interest from Theorists

The measurement proposed has stirred interest in a number of theorists who either have provided or are currently working on calculations. A few of these remain on-going and are expected to be completed in the near future.

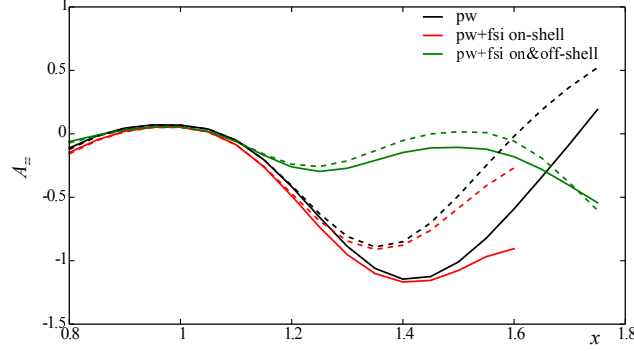


Figure 8: Same as Fig. 7, but for $E_0 = 8.8 \text{ GeV}^2$ and $Q^2 = 2.9 (\text{GeV}/c)^2$.

The light cone and virtual nucleon calculations of M. Sargsian [32] and M. Strikman [39] are available for A_{zz} and are presented in this document. Calculations have been done with different NN potentials and have found significant differences at large x .

Continuing his interest from DIS b_1 calculations [36], W. Cosyn has developed calculations of the quasi-elastic contribution to inclusive deuteron scattering, which will be the dominant contribution in the $x > 1$ regime [37]. His calculations, which include final-state interactions, have been modified to include A_{zz} and are presented in this proposal.

Calculations of both relativistic plane-wave Born approximation and calculations including meson-exchange currents, isobar currents, and relativistic effects were provided by H. Arenhovel [21, 40] for all of our kinematic settings. He also provided calculations for the unpolarized and vector polarized observables that demonstrate why a tensor polarized target is necessary to reach the physics goals of this experiment.

G. A. Miller [41] has developed an interest in this measurement, and has done recent work investigating the relativistic components of the deuteron wave-function, including making predictions for A_{zz} [28]. His paper also states that, “Presently there is a strong need for models of the deuteron wave function that are both realistic and relativistic” and notes that this proposal for A_{zz} is the only current experiment planned to specifically test between relativistic deuteron calculations. In his own words, he states “This proposal really challenges theorists to better understand the meaning of nuclear wave functions in a situation that demands a relativistic treatment.”

Although not completed at the time of submission, W. Van Orden has calculations in progress using different nucleon-nucleon potentials, as well as different prescriptions for handling the reactions mechanisms in the low Q^2 region for tensor polarization observables. In his words, “Recent studies have shown that it is extremely challenging to disentangle reaction mechanisms from nucleon-nucleon potential effects using cross section information [10]. This group is now in the process of extending their studies to vector and tensor asymmetries. Previous low Q^2 measurements seemed to indicate that the asymmetries are far less sensitive to reaction mechanisms than the cross sections [9]; so while the new calculations are not yet available, it is clear that the asymmetries will produce unique constraints on our understanding of the deuteron.” [8]

S. Liuti also affirms the importance of understanding the structure of the deuteron in the kine-

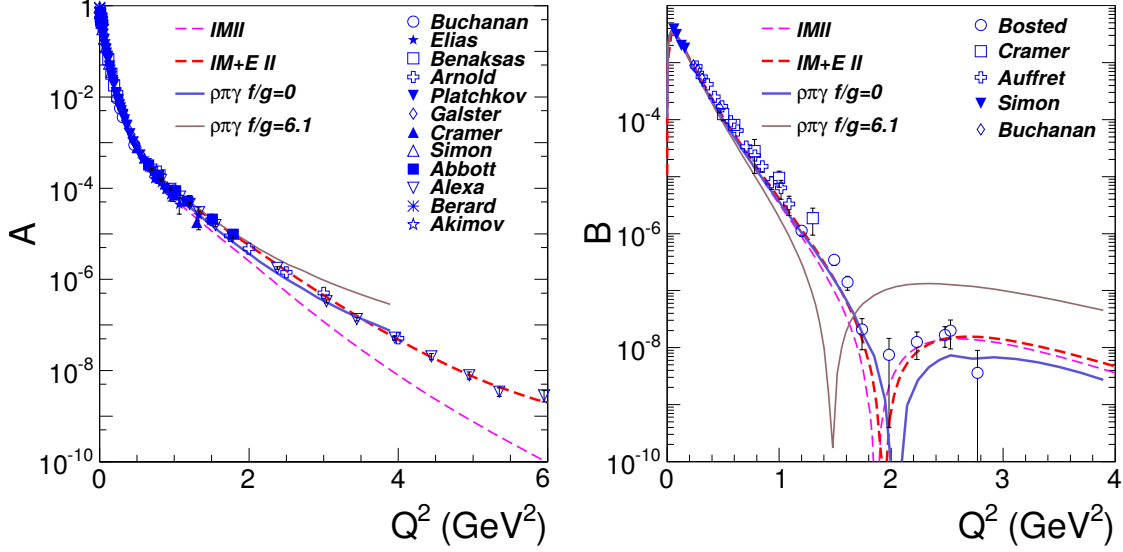


Figure 9: World data on the unpolarized deuteron form factors A and B [43].

matics presented in this proposal, stating “This is an important measurement and should be calculated more thoroughly.” [42]

In summary, we are encouraged that several theorists have been and continue to be engaged in serious efforts to calculate A_{zz} in the $x > 1$ region using a variety of models.

2 T_{20} Motivation

The elastic cross section of the deuteron is described by the charge (G_C), magnetic (G_M), and quadrupole (G_Q) form factors. In order to access all three form factors, measurements are needed for both polarized and unpolarized cross sections.

In the unpolarized case, the cross section is determined by

$$\frac{d\sigma}{d\Omega} = \frac{d\sigma}{d\Omega}\Big|_{NS} \left[A(Q^2) + B(Q^2) \tan^2 \frac{\theta}{2} \right], \quad (4)$$

where A and B are related to the charge (G_C), magnetic (G_M), and quadrupole (G_Q) form factors by

$$A = G_C^2(Q^2) + \frac{8}{9}\eta^2 G_Q^2 + \frac{2}{3}\eta G_M^2(Q^2), \quad (5)$$

$$B = \frac{4}{3}\eta(1 + \eta)G_M^2(Q^2), \quad (6)$$

where $\eta = Q^2/4M^2$. The A and B form factors have been measured to high precision by many experiments, as shown in Fig. 9

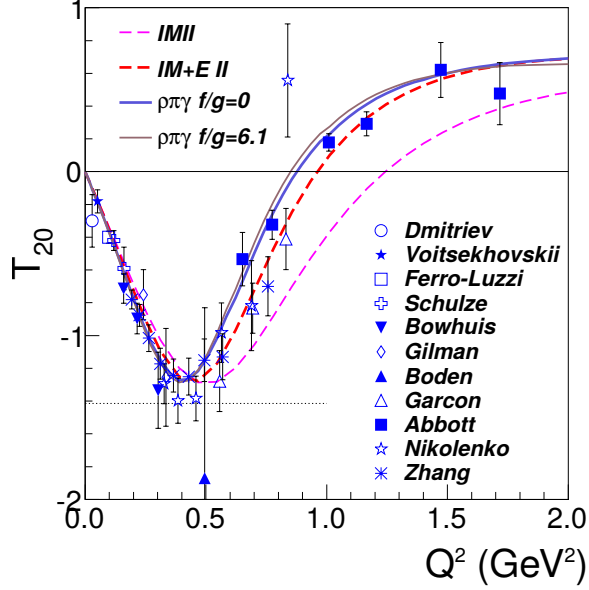


Figure 10: Existing world data on the tensor analyzing power T_{20} [43].

In order to separate out all three form factors, a measurement of the tensor analyzing powers is also needed. Although a number of tensor analyzing powers are available, T_{20} has proven to be the most informative and has been studied more in depth than the others. This analyzing power is defined by

$$T_{20} = -\frac{\frac{8}{9}\eta^2 G_Q^2 + \frac{8}{3}\eta G_C G_q + \frac{2}{3}\eta G_M^2 \left[\frac{1}{2} + (1 + \eta) \tan^2(\theta/2) \right]}{\sqrt{2}[A + B \tan^2(\theta/2)]}, \quad (7)$$

and can be measured by knowing either the initial or final polarization state. With measurements of A , B , and T_{20} , each of the three deuteron form factors can be extracted.

As shown in Fig. 10, the world data for T_{20} is far less well-measured than A and B . There are systematic discrepancies present between the different datasets, with measurements from JLab coming out less negative than those from Bates and VEPP-3 at higher $Q^2 > 0.5 \text{ GeV}^2$, which affects model calculations particularly for determining G_C [44]. Additionally, only a single experiment has been done for large $Q^2 > 1 \text{ GeV}^2$ [45], and more data is needed in order to confirm our present understanding of T_{20} .

One of the leading uncertainties that will effect all tensor polarized deuterium experiments is the absolute knowledge of the tensor polarization. We have found that by using the elastic reaction at low Q^2 , we can normalize our target's degree of polarization to the high-precision low Q^2 NIKHEF T_{20} measurement. The NIKHEF tensor polarization was created with an atomic beam source and they were able to measure the polarization of the gas with both a Breit-Rabi polarimeter as well as an ion-extraction polarimeter [46].

An ideal measurement of T_{20} would be taken over a large range of Q^2 , which could use the lower $Q^2 < 0.4 \text{ GeV}^2$ results to make sure that systematic uncertainties are well understood while

simultaneously measuring the region of current discrepancies ($Q^2 \approx 0.75 \text{ GeV}^2$) and extending to larger four-momentum transfer to confirm the single measurement taken at $Q^2 > 1 \text{ GeV}^2$. By utilizing the same time-frame, kinematics, and equipment that will be used to determine A_{zz} , we propose such a measurement.

3 The Proposed Experiment

We propose to measure the tensor asymmetry A_{zz} and tensor analyzing power T_{20} from inclusive electron scattering from polarized deuterons in the quasi-elastic and elastic region of $0.30 < x < 2.0$, $0.2 (\text{GeV}/c)^2 < Q^2 < 2.9 (\text{GeV}/c)^2$, and $1.8 < W_{NN} < 3.1 \text{ GeV}$ using the Hall C HMS and SHMS spectrometers at forward angle and a solid polarized ND_3 target.

3.1 A_{zz} Experimental Method

The measured double differential cross section for electron scattering from a spin-1 target is characterized by a vector polarization P_z and tensor polarization P_{zz} . With an unpolarized beam and the target field oriented along the beam, the cross section is expressed as [21]

$$\frac{d^2\sigma_p}{d\Omega dE'} = \frac{d^2\sigma_u}{d\Omega dE'} \left(1 + \frac{1}{2} P_{zz} A_{zz} \right), \quad (8)$$

where σ_p (σ_u) is the polarized (unpolarized) cross section and A_{zz} is the tensor asymmetry of the virtual-photon deuteron cross section. This allows us to write the polarized tensor asymmetry with positive tensor polarization using an unpolarized electron beam as

$$A_{zz} = \frac{2}{P_{zz}} \left(\frac{\sigma_p - \sigma_u}{\sigma_u} \right). \quad (9)$$

The tensor polarization is given by

$$P_{zz} = (p_+ + p_-) - 2p_0, \quad (10)$$

where p_m represents the population in the $m_J = +1, -1$, or 0 state.

Eq. 9 reveals that the asymmetry A_{zz} compares two different cross sections measured under different polarization conditions of the target: positively tensor polarized and unpolarized. To obtain the relative cross section measurement in the same configuration, the same target cup and material will be used at alternating polarization states (polarized vs. unpolarized), and the magnetic field providing the quantization axis will be oriented along the beamline at all times. This field will always be held at the same value, regardless of the target material polarization state. This process, identical to that used for the already-approved b_1 measurement [47], ensures that the acceptance remains consistent within the stability of the superconducting magnet. To better agree with theory calculations, the value of A_{zz} will be rotated to be along the \vec{q} vector.

Since many of the factors involved in the cross sections cancel in the ratio, Eq. 9 can be expressed in terms of the charge normalized, efficiency corrected numbers of tensor polarized

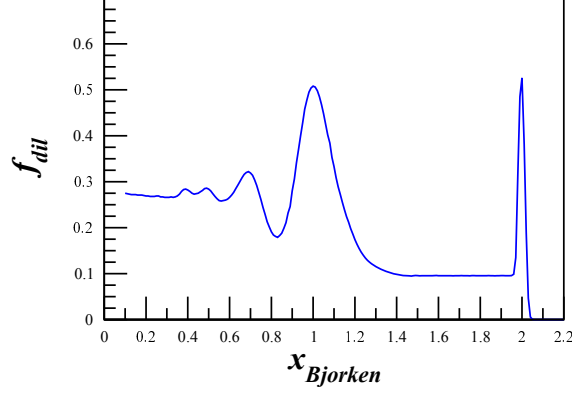


Figure 11: The estimated dilution factor, in this case at $Q^2 = 1.5 \text{ (GeV}/c)^2$, is expected to drop off at high x until it reaches the SRC plateau region and then the elastic peak at $x = 2$. The low dilution factor of $1.1 < x < 1.95$ will be counteracted by using a high-luminosity target.

(N_p) and unpolarized (N_u) counts,

$$A_{zz} = \frac{2}{fP_{zz}} \left(\frac{N_p - N_u}{N_u} \right). \quad (11)$$

The dilution factor f corrects for the presence of unpolarized nuclei in the target and is defined by

$$f = \frac{N_D \sigma_D}{N_N \sigma_N + N_D \sigma_D + \sum_A N_A \sigma_A}, \quad (12)$$

where N_D is the number of deuterium nuclei in the target and σ_D is the corresponding inclusive double differential scattering cross section, N_N is the nitrogen number of scattered nuclei with cross section σ_N , and N_A is the number of other scattering nuclei of mass number A with cross section σ_A . As has been noted in previous work [6], the dilution factor at high x drops off considerably until the SRC plateau region, as shown in Fig. 11. By using a high-luminosity solid target at a small scattering angle $\theta_{e'}$, this effect will be counteracted. The dilution factor is a much smaller problem for elastic deuteron scattering at $x = 2$.

The dilution factor can be written in terms of the relative volume ratio of ND_3 to LHe in the target cell, otherwise known as the packing fraction p_f . In our case of a cylindrical target cell oriented along the magnetic field, the packing fraction is exactly equivalent to the percentage of the cell length filled with ND_3 .

If the time is evenly split between scattering off of polarized and unpolarized ND_3 , the time necessary to achieve the desired precision δA is:

$$t = \frac{N_p}{R_p} + \frac{N_u}{R_u} = \frac{8}{f^2 P_{zz}^2} \left(\frac{R_p (R_u + R_p)}{R_u^3} \right) \frac{1}{\delta A_{zz}^2} \quad (13)$$

where $R_{p(u)}$ is the polarized (unpolarized) rate and $N_{p(u)}$ is the total estimated number of polarized (unpolarized) counts to achieve the uncertainty δA_{zz} .

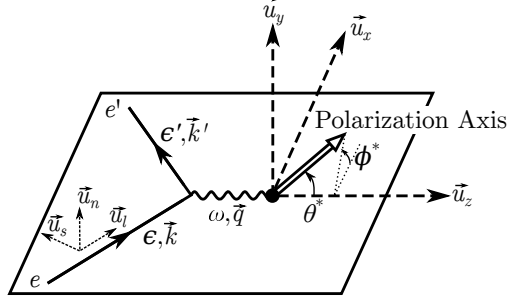


Figure 12: Coordinate system used in determining the tensor analyzing powers.

3.2 T_{20} Experimental Method

A measurement of T_{20} will be extracted from A_{zz} on the elastic peak for each Q^2 mentioned in Section 3.3. We will follow the method described by the NIKHEF measurements [46], which also used a tensor polarized target. Our methods differ in that we will use the high angular and energy resolution of each Hall C spectrometer to determine elastic deuteron scattering through kinematic cuts, where NIKHEF utilized two non-magnetic detectors to measure the scattered electron and recoil deuteron in coincidence.

The analyzing powers of a tensor-polarized target are described by the cross-section

$$\sigma = \sigma_0 \left[1 + \frac{A_d^T P_{zz}}{\sqrt{2}} \right], \quad (14)$$

where

$$A_d^T = \sum_{i=0}^2 d_{2i} T_{2i} \quad (15)$$

and

$$d_{20} = \frac{3 \cos^2 \theta^* - 1}{2}, \quad d_{21} = -\sqrt{\frac{3}{2}} \sin 2\theta^* \cos \phi^*, \quad d_{22} = \sqrt{\frac{3}{2}} \sin^2 \theta^* \cos 2\phi^*. \quad (16)$$

θ^* and ϕ^* are in the frame where the z axis is along the \vec{q} and the x axis is perpendicular to z in the scattering plane, as described in [48] and shown in Fig. 12. For this proposal, $\theta^* \approx 70^\circ$ and $\phi^* \approx 0^\circ$, as our target field will be oriented along the beamline and $\theta_{\vec{q}} \approx 70^\circ$ on the elastic peak.

We rearrange Eq. 14 to be defined as our observable $A_{zz} = \frac{2}{P_{zz}} \left(\frac{\sigma}{\sigma_0} - 1 \right)$,

$$A_{zz} = \sqrt{2} [d_{20} T_{20} + d_{21} T_{21} + d_{22} T_{22}], \quad (17)$$

$$T_{20} = \frac{A_{zz}}{d_{20} \sqrt{2}} - \frac{d_{21}}{d_{20}} T_{21} - \frac{d_{22}}{d_{20}} T_{22}. \quad (18)$$

Contributions from T_{21} and T_{22} are expected to be small but not negligible, and will be calculated from models that best match world data. Uncertainties from T_{21} and T_{22} are expected to be 10% and are included within the T_{20} systematic calculations.

		E_0 (GeV)	Q^2 (GeV ²)	E' (GeV)	$\theta_{e'}$ (°)	Rates (kHz)	PAC Time (Days)
SHMS	(S1)	8.8	1.5	8.36	8.2	0.38	25
HMS	(H1)	8.8	2.9	7.26	12.2	0.04	25
SHMS	(S2)	6.6	0.7	6.35	7.5	3.57	8
HMS	(H2)	6.6	1.8	5.96	12.3	0.09	8
SHMS	(S3)	2.2	0.2	2.15	10.9	10.5	1
HMS	(H3)	2.2	0.3	2.11	14.9	3.23	1

Table 1: Summary of the central kinematics and physics rates using the Hall C spectrometers.

3.3 Kinematics

We propose to measure the tensor asymmetry A_{zz} for $0.30 < x < 2.0$, $0.2 \text{ (GeV}/c)^2 < Q^2 < 2.9 \text{ (GeV}/c)^2$, and $1.8 < W_{NN} < 3.1 \text{ GeV}$ and extract the tensor analyzing power T_{20} for $0.2 \text{ (GeV}/c)^2 < Q^2 < 1.8 \text{ (GeV}/c)^2$. Central kinematics of the spectrometers are given in Table 1. Fig. 13 shows the planned kinematic coverage utilizing the Hall C HMS and SHMS spectrometers at forward angles.

Although it has been pointed out that the current construction of the SHMS constrains it to angles $> 10^\circ$ due to fringe fields affecting the beam entering the dump [49], this can be resolved in a number of ways. As discussed in [49], passive iron shielding can be installed within the SHMS that would not affect the target field. Additionally, given the low beam current proposed, a local beam dump could be installed immediately following the target. In the worst case, we could meet the physics motivation by keeping the same Q^2 ranges as S1, S2, and S3 but lowering the highest beam energies while putting the SHMS at larger angles. In this case, the HMS would be used at very similar angles to combine statistics between the spectrometers to make up for the loss in statistics from the SHMS.

The polarized ND₃ target is discussed in Section 3.5. The magnetic field of the target will be held longitudinally along the beamline at all times, while the target state is alternated between a polarized and unpolarized state. The field will alternate between parallel and anti-parallel with each re-polarization to reduce systematic effects from vector polarization. The tensor polarization and packing fraction used in the rates estimate are 30% and 0.65, respectively. The dilution factor in the range of this measurement is shown in Fig. 14. The spread of the elastic peak for the dilution factor was calculated assuming a momentum resolution of 0.1% for the HMS and 0.08% for the SHMS. With an incident electron beam current of 80 nA, the expected deuteron luminosity is $1.2 \times 10^{35} \text{ cm}^{-2}\text{s}^{-1}$. Experiments that have previously run at a similar current include SANE (E07-003), RSS (E01-006), and GEN (E93-026).

The momentum bite and the acceptance were assumed to be $\Delta P = \pm 8\%$ and $\Delta\Omega = 5.6 \text{ msr}$ for the HMS, and $\Delta P = {}^{+20\%}_{-8\%}$ and $\Delta\Omega = 4.4 \text{ msr}$ for the SHMS. For the choice of the kinematics, special attention was taken onto the angular and momentum limits of the spectrometers with a longitudinal polarized target: for the HMS, $12.2^\circ \leq \theta \leq 85^\circ$ and $1 \leq P_0 \leq 7.3 \text{ GeV}/c$, and for the SHMS, $5.5^\circ \leq \theta \leq 40^\circ$ and $2 \leq P_0 \leq 11 \text{ GeV}/c$. In addition, the opening angle between the

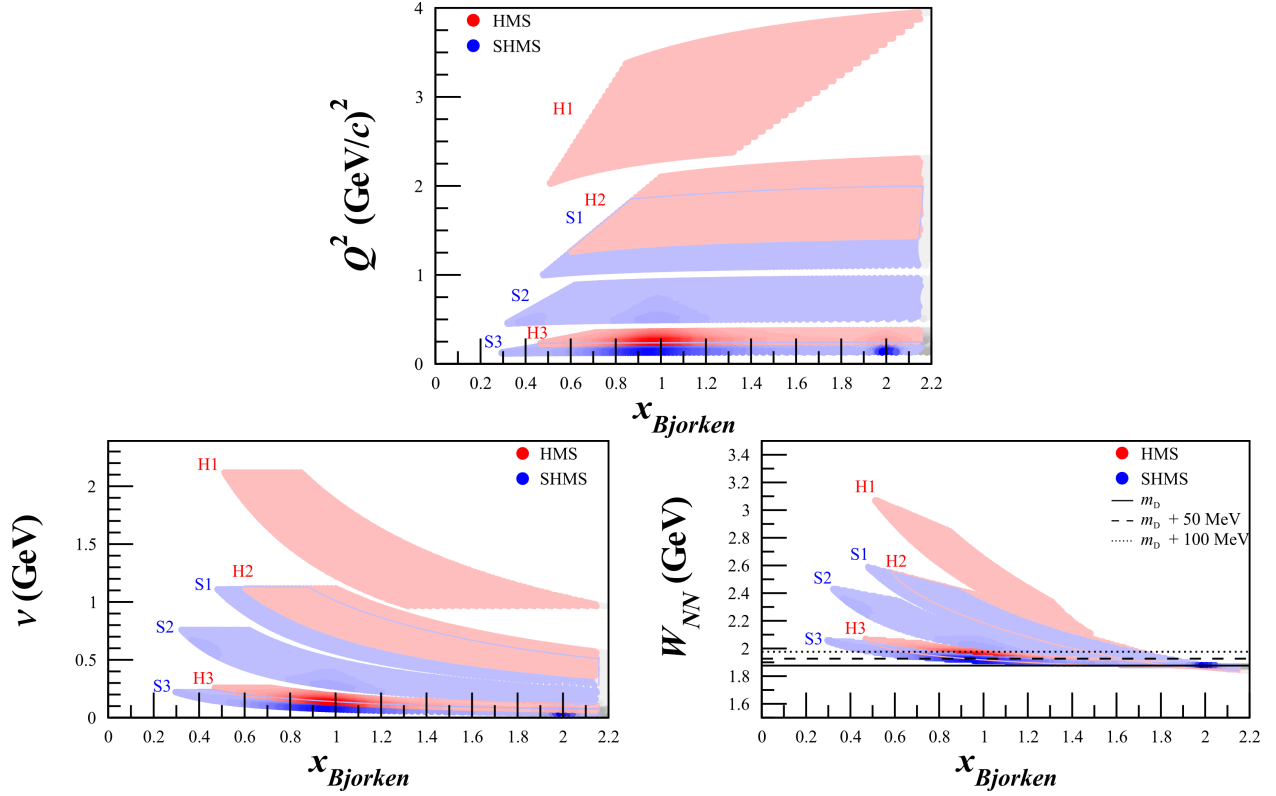


Figure 13: Kinematic coverage for central spectrometer settings at $Q^2 = 2.9$ (GeV/c)² (H1), 1.8 (GeV/c)² (H2), 1.5 (GeV/c)² (S1), 0.7 (GeV/c)² (S2), 0.3 (GeV/c)² (H3), and 0.2 (GeV/c)² (S3). The grey regions are not included in our statistics estimates since they fall outside the range of electron-deuteron scattering. Darker shading represents areas with higher statistics. The solid, dashed, and dotted lines in the W_{NN} plot indicate deuteron mass, deuteron mass + 50 MeV, and deuteron mass + 100 MeV, respectively. Differences from final state interactions in virtual nucleon and light cone calculations are minimized for $W_{NN} > m_D + 50$ MeV [12].

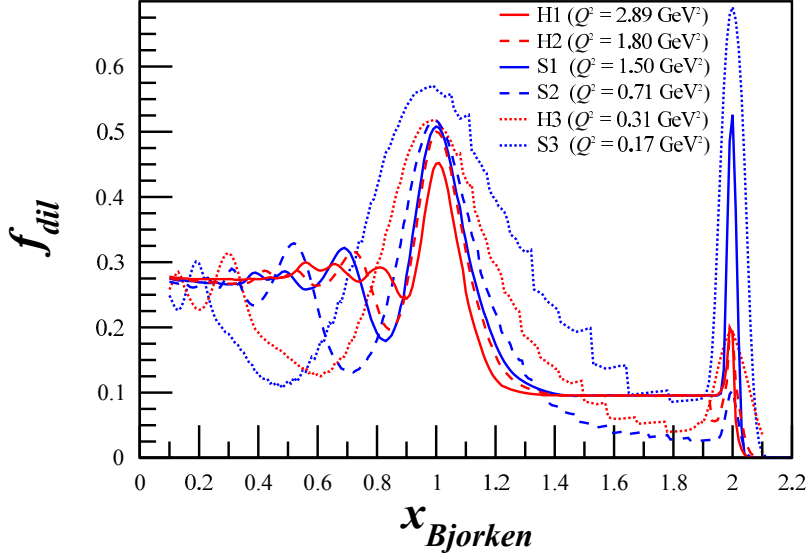


Figure 14: Projected dilution factor covering the entire x range to be measured using a combination of P. Bosted’s [50] and M. Sargsian’s [32] code, along with a calculation of the elastic peak using a parametrization of the deuteron form factors, for each of the kinematic settings described in Table 1.

spectrometers is physically constrained to be larger than 17.5° .

A total of 34 days of beam time is requested for production data, with an additional 11 days of expected overhead. The expected uncertainties, described in detail in Section 3.4, are given in Tables 2-4 and Figs. 15-17.

3.4 Uncertainty Estimates

We discuss here the expected statistical and systematic uncertainties that we expect to contribute to the measurement. The projected uncertainties for A_{zz} are summarized in Tables 2-3 and displayed in Fig. 15. The projected uncertainties for T_{20} are summarized in Table 4 and displayed in Fig. 16.

The uncertainties for kinematic setting S1 are also shown in Fig. 17 where all calculations are normalized to the Light Cone AV-18 calculation. This was done to emphasize the discriminating power of our expected data in a region with an extremely large range of predicted outcomes. Fig. 17 also highlights the unique capability of this experiment to distinguish between relativistic calculations at $x < 1.3$ with a discriminating power of greater than 6σ before the wavefunction inputs diverge, at which point the most predictive model at low x can be used to distinguish between hard and soft wavefunctions at $x > 1.3$ with a discriminating power of up to $> 4\sigma$.

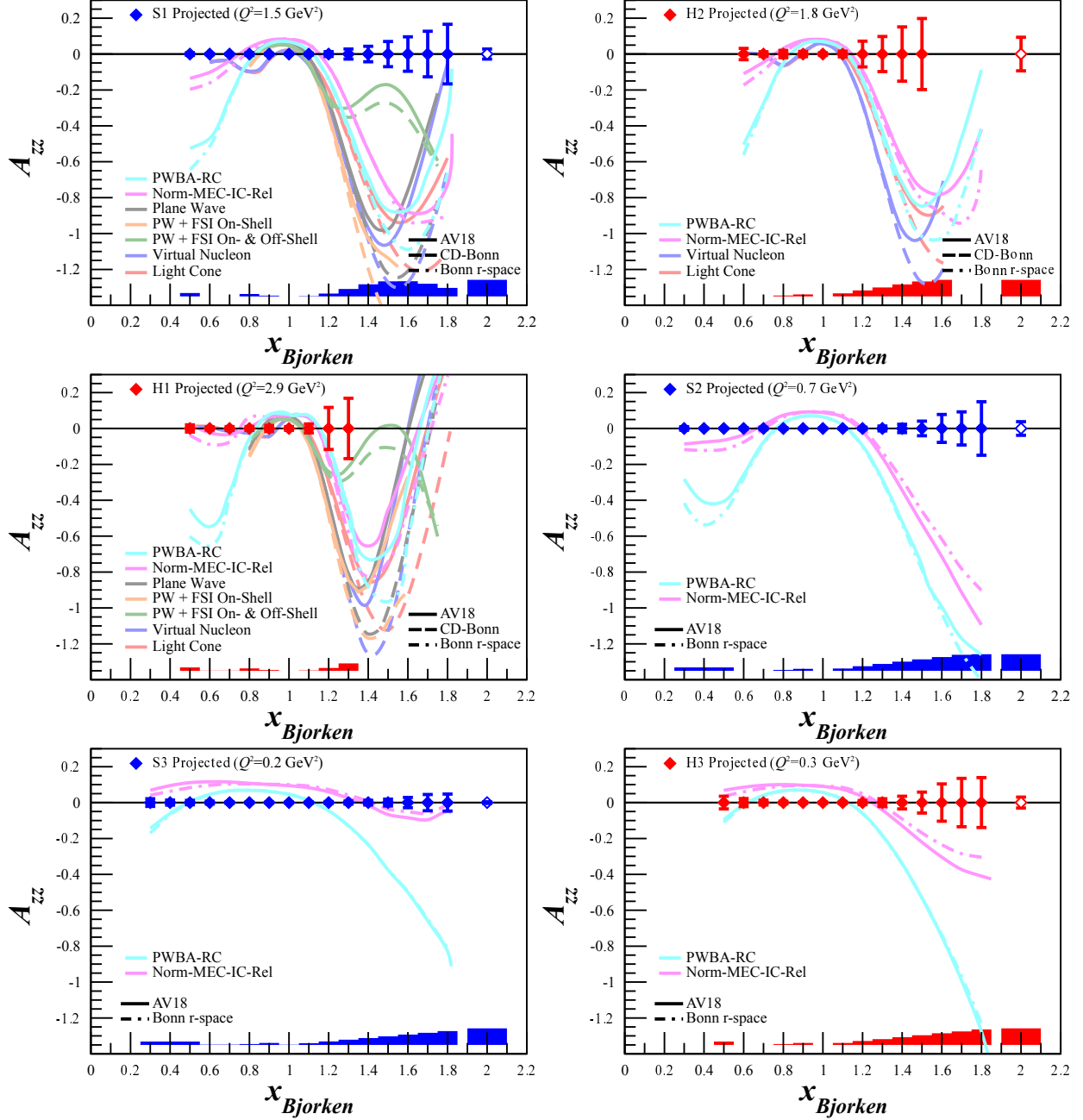


Figure 15: Projected uncertainties for the tensor asymmetry A_{zz} with 34 days of beam time for SHMS settings S1, S2, and S3, and HMS settings H1, H2, and H2 as described in Table 1. Filled points represent quasi-elastic data and open points represent elastic data. The bottom band represents the systematic uncertainty. The upper x limit for H1 (H2) is $x = 1.3$ ($x = 1.5$). Light-cone (LC) and virtual-nucleon (VN) calculations using the AV18 and CD-Bonn potentials were provided by M. Sargsian [7]. The threshold of $W_{NN} > m_D + 50$ MeV is at $x \approx 1.75$ for the higher Q^2 points S1, H1, and H2. Below this, effects of FSI on VN and LC calculations are minimized [12]. Final state interactions on the virtual-nucleon model were provided by W. Cosyn [37], indicating the effects from on- and off-shell.

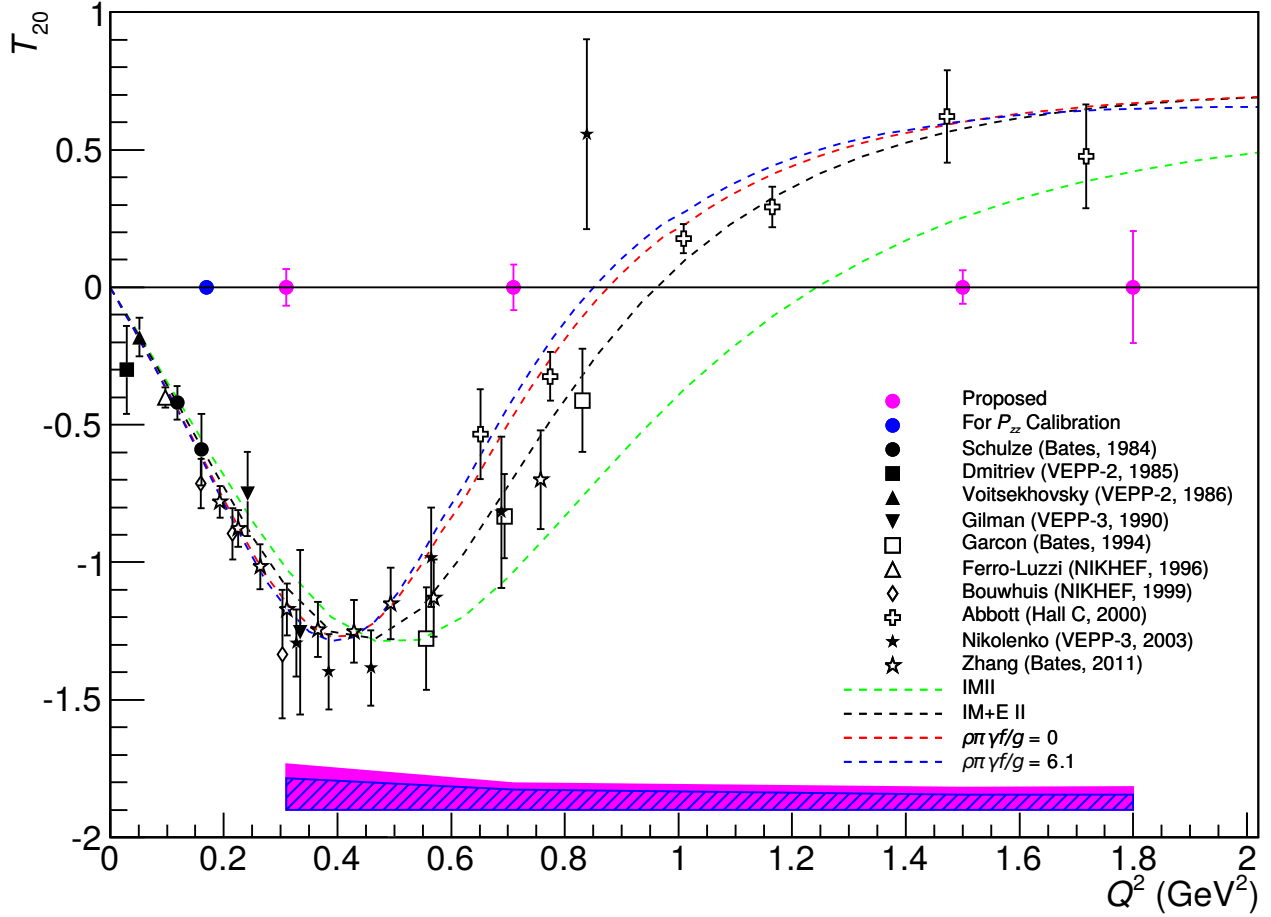


Figure 16: Projected uncertainties for the elastic tensor analyzing power T_{20} with 34 days of beam time are shown alongside the world data [43]. The point shown in blue, measured at $Q^2 = 0.2 \text{ GeV}^2$ where T_{20} is well known theoretically and experimentally, will be used as a calibration for P_{zz} , and can potentially be used to further reduce the leading systematic uncertainty as indicated by the blue-dashed band.

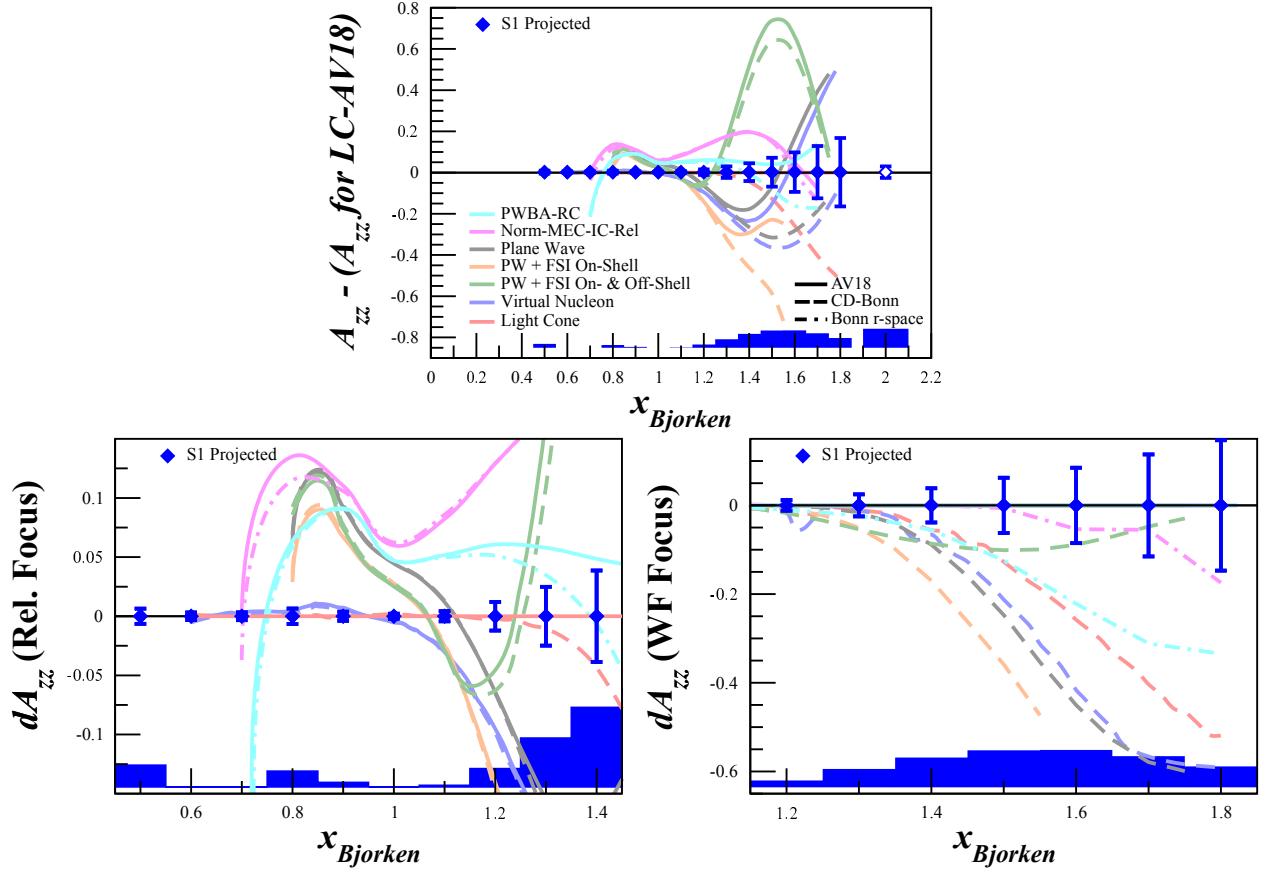


Figure 17: All calculations in the top and bottom-left plots have been subtracted by the Light Cone AV-18 calculation. LC-AV18 was arbitrarily selected as one of the most central calculations to allow for an easier comparison of the discriminating power of the data, particularly for the calculations with low or no contributions from off-shell FSI (all but green), which is expected from the choice of kinematics. The top plot shows the entire S1 kinematic range, while the bottom-left plot zooms on the region of $0.45 < x < 1.45$ to highlight the region where we have excellent sensitivity ($> 6\sigma$) to discriminate different relativistic models before the wavefunctions begin to diverge at $x \approx 1.3$. By determining which model type is correct in the low x region, we can focus on that model to determine between deuteron wavefunctions at higher x . In the bottom-right plot, all AV-18 calculations are set to zero and each Bonn calculation was subtracted by its corresponding AV-18 calculation. This shows how well we can discriminate between hard and soft wavefunctions (up to $> 4\sigma$) for each calculation at large x after determining which relativistic model is most predictive at lower x .

x	H1: $Q^2 = 2.9 \text{ (GeV}/c)^2$			H2: $Q^2 = 1.8 \text{ (GeV}/c)^2$			S1: $Q^2 = 1.5 \text{ (GeV}/c)^2$		
	f_{dil}	δA_{zz}^{stat} $\times 10^{-2}$	δA_{zz}^{sys} $\times 10^{-2}$	f_{dil}	δA_{zz}^{stat} $\times 10^{-2}$	δA_{zz}^{sys} $\times 10^{-2}$	f_{dil}	δA_{zz}^{stat} $\times 10^{-2}$	δA_{zz}^{sys} $\times 10^{-2}$
0.50	0.29	2.02	1.84	—	—	—	0.25	0.72	1.84
0.60	0.29	0.91	0.10	0.27	3.15	0.10	0.30	0.36	0.10
0.70	0.27	1.01	0.10	0.32	1.26	0.10	0.29	0.38	0.10
0.80	0.30	1.11	1.34	0.20	2.00	0.48	0.17	0.74	1.34
0.90	0.24	1.73	0.38	0.27	1.45	1.10	0.29	0.44	0.38
1.00	0.46	1.03	0.10	0.50	0.74	0.10	0.51	0.24	0.10
1.10	0.28	2.48	0.14	0.33	1.58	1.65	0.34	0.49	0.14
1.20	0.09	11.7	1.55	0.10	7.18	3.31	0.17	1.34	1.55
1.30	0.11	16.8	4.13	0.11	9.76	4.96	0.12	2.79	4.13
1.40	—	—	—	0.12	15.1	6.65	0.13	4.30	6.72
1.50	—	—	—	0.11	19.8	8.29	0.10	7.01	8.34
1.60	—	—	—	—	—	—	0.10	9.60	8.42
1.70	—	—	—	—	—	—	0.10	12.7	7.04
1.80	—	—	—	—	—	—	0.10	16.6	4.72
2.00	—	—	—	0.20	9.33	9.20	0.50	2.79	9.20

Table 2: Summary of the expected uncertainty for each x bin for settings S1, H1, and H2.

3.4.1 Statistical Uncertainty

To investigate the statistical uncertainty we start with the equation for A_{zz} using measured counts for polarized data (N_p) and unpolarized data (N_u),

$$A_{zz} = \frac{2}{fP_{zz}} \left(\frac{N_p}{N_u} - 1 \right). \quad (19)$$

The statistical error with respect to counts is then

$$\delta A_{zz} = \frac{2}{fP_{zz}} \sqrt{\left(\frac{\delta N_p}{N_u} \right)^2 + \left(\frac{N_p \delta N_u}{N_u^2} \right)^2}. \quad (20)$$

For $\delta N_{p(u)} = \sqrt{N_{p(u)}}$, the uncertainty becomes

$$\delta A_{zz} = \frac{2}{fP_{zz}} \sqrt{\frac{N_p(N_u + N_p)}{N_u^3}}, \quad (21)$$

which can't be simplified further due to the large expected asymmetry.

The number of counts was calculated using a combination of P. Bosted's [50] and M. Sargsian's [32] code for $x < 2$. The Bosted code was used for the lowest Q^2 setting, where effects of SRC scaling

x	S2: $Q^2 = 0.7 \text{ (GeV/c)}^2$			H3: $Q^2 = 0.3 \text{ (GeV/c)}^2$			S3: $Q^2 = 0.2 \text{ (GeV/c)}^2$		
	f_{dil}	δA_{zz}^{stat} $\times 10^{-2}$	δA_{zz}^{sys} $\times 10^{-2}$	f_{dil}	δA_{zz}^{stat} $\times 10^{-2}$	δA_{zz}^{sys} $\times 10^{-2}$	f_{dil}	δA_{zz}^{stat} $\times 10^{-2}$	δA_{zz}^{sys} $\times 10^{-2}$
0.30	0.24	0.99	1.84	—	—	—	0.18	2.13	1.84
0.40	0.28	0.26	1.84	—	—	—	0.12	1.38	1.84
0.50	0.32	0.21	1.84	0.14	3.52	1.84	0.11	1.23	1.84
0.60	0.19	0.41	0.10	0.12	2.26	0.10	0.18	0.78	0.10
0.70	0.13	0.68	0.10	0.18	1.33	0.10	0.28	0.48	0.10
0.80	0.19	0.48	0.48	0.30	0.72	0.48	0.42	0.31	0.48
0.90	0.39	0.22	1.10	0.46	0.45	1.10	0.54	0.24	1.10
1.00	0.52	0.16	0.10	0.52	0.43	0.10	0.58	0.25	0.10
1.10	0.39	0.28	1.27	0.43	0.63	1.07	0.53	0.33	0.95
1.20	0.22	0.65	2.54	0.30	1.15	2.14	0.40	0.55	1.91
1.30	0.14	1.34	3.81	0.19	2.16	3.22	0.32	0.83	2.87
1.40	0.09	2.29	5.06	0.14	3.52	4.29	0.24	1.31	3.82
1.50	0.06	4.09	6.35	0.10	5.85	5.37	0.20	1.86	4.78
1.60	0.04	7.76	7.60	0.06	10.4	6.45	0.14	2.87	5.74
1.70	0.04	9.23	8.88	0.05	13.5	7.52	0.10	4.53	6.69
1.80	0.03	14.9	9.20	0.06	13.9	8.60	0.11	4.73	7.66
2.00	0.67	3.79	9.20	0.20	3.05	9.20	0.70	0.45	9.20

Table 3: Summary of the expected uncertainty for each x bin for settings S2, S3, and H3.

Setting	Q^2 (GeV^2)	δT_{20}^{stat} $\times 10^{-2}$	δT_{20}^{sys} $\times 10^{-2}$
H2	1.8	21.7	4.74
S1	1.5	6.09	4.77
S2	0.7	8.28	6.88
H3	0.3	6.66	9.91
S3	0.2	0.99	5.59

Table 4: Expected uncertainties for T_{20} assuming a systematic uncertainty of 9.2%, which could be reduced further by utilizing the S3 measurement as a calibration for the polarized target.

are expected to be negligible, and for $x < 1.1$ to accurately determine the quasi-elastic peak. The Sargsian code was used for the higher Q^2 settings at $x > 1.1$ due to its inclusion of SRC scaling effects.

The deuteron elastic peak was calculated using a parametrization of the deuteron elastic form factors A and B by

$$\frac{d^2\sigma}{d\Omega dE'} = \sigma_{\text{Mott}} \left(\frac{E'}{E} \right) \left[A + B \tan^2 \left(\frac{\theta}{2} \right) \right] \delta(E' - E'_{el}), \quad (22)$$

where $\delta(E' - E'_{el})$ is approximated by a Gaussian distribution with its width determined by the resolution of the spectrometers,

$$\delta(E' - E'_{el}) = \frac{1}{2\Delta E \cdot E'_{el}\sqrt{\pi}} e^{-\frac{(E' - E'_{el})^2}{2(\Delta E \cdot E'_{el})^2}}, \quad (23)$$

where $\Delta E = 0.1$ (0.08)% for the HMS (SHMS) and $E'_{el} = \frac{Q^2}{2m_D}$. This was added to the rates calculation that was used for quasi-elastic A_{zz} and b_1 [51], and the uncertainty of A_{zz} on the elastic peak was calculated as in Eq. 21.

Following the methodology discussed in Section 3.2, we obtain the following uncertainties for T_{20} :

$$\delta T_{20}^{stat} = \frac{\delta A_{zz}^{stat}}{d_{20}\sqrt{2}}, \quad (24)$$

$$\delta T_{20}^{sys} = \sqrt{\left(\frac{\delta A_{zz}^{sys}}{d_{20}\sqrt{2}} \right)^2 + \left(\frac{d_{21}}{d_{20}} \delta T_{21} \right)^2 + \left(\frac{d_{21}}{d_{20}} \delta T_{22} \right)^2}. \quad (25)$$

3.4.2 Systematic Uncertainty

The spin-1 tensor-polarization dependent observables are part of the family of asymmetries which relies on obtaining data for two different target helicity states under equivalent experimental settings. A large contribution of the experimental uncertainty that effects absolute normalization cancels out as terms in the denominator and numerator are equivalent. For situations where the experimental configuration has changed during the data collection of the two different helicity states the cancellation does not occur and a rigorous accounting of the errors is required.

The tensor-polarization dependent asymmetry takes the form

$$A_{zz} = \frac{2}{fP_{zz}} \left(\frac{\sigma_p}{\sigma_u} - 1 \right), \quad (26)$$

where σ_p is the polarized cross section and σ_u is the unpolarized cross section. There are of course other spin-1 alignment dependent asymmetries, but for positive quadruple polarization in inclusive scattering all polarized observables can be expressed in terms of A_{zz} .

The contributions to the experimental uncertainty come from inaccuracies inherent in the system of measurement of the observable of interest. Each experiment contains instrumental components of systematic error which may or may not have dependence on accessible parameters. These

types of errors can have a nonzero mean that changes over time so that its effect is not reduced when observations are averaged. There are also stochastic components to the uncertainty which will vary only around a single mean. There may still be a time dependence to the standard deviation of the stochastic contributions but these types of errors can be reliably estimated by repeating measurements.

Monitoring the systemic coupling of the instrumental parameters can greatly reduce the overall uncertainty produced in small asymmetry measurements. An understanding of the evolution of these types of errors over the course of the experiment can be used to make corrections after data acquisition. Reducing the time in each target spin orientation can also significantly reduce the impact of shifts in normalization. However, the stochastic components must be regulated prior to and during the experiment. Helicity flips can not reduce this type of uncertainty contribution.

Many of the errors that arise from limitations in measurement capacity have a statistical probability distribution that can be accurately estimated. For many of these types of uncertainties it is possible to derive confidence limits on the domain of the measured value resulting in a relative contribution to the total systematic error. Under an independent error assumption these relative contributions add in quadrature, with polarization being the dominating uncertainty in the spin dependent observables. The standard law of combination of errors does not work when there are correlations between these types of uncertainties. For this situation the full covariance matrix is required and a minimization procedure maybe needed to keep the error under control. This is only relevant for dominant errors. For multiple kinematic tracking variables strict estimation and handling of each uncertainty is essential for a complete analysis. In many cases one may wish to assume 100% correlation between variables to simplify the book keeping for smaller contributions.

Errors are often assumed to have a normal distribution. In reality measurement errors are rarely distributed in a true Gaussian and usually have some prominent non-Gaussian tail. Given a sufficient number of measurements the central limit theorem can be employed to ensure that the estimated parameters will be more Gaussian than the estimated measurements.

Table 5 shows a list of the scale dependent uncertainties contributing to the systematic error in A_{zz} .

Polarization error is well understood and steps will be taken to minimize these contributions, as has been done in previous experiments [52]. There are additional uncertainties that can arise from RF quadrupole polarization enhancement, but recent efforts by the UVA target group to study the tensor-enhanced NMR line-shape indicate that the total uncertainty in this case can be held under 6% [53, 54]. The figure of merit (FOM) for a tensor polarized solid state target can be defined as,

$$FOM = n_t f^2 P_{zz}^2 \quad (27)$$

where n_t is the target thickness and P_{zz} is the tensor polarization.

The dilution factor f varies as a function of scattered electron energy, particularly at kinematics where nucleon resonances are prominent. The dilution factor must be known precisely at each kinematic point. This factor must be based on empirical information with measurable error, which will be measured multiple times at each kinematic setting. Though the loss to the figure of merit can easily be recovered for lower f , the error calculated from the variation of the models is only a crude estimate.

Source	A_{zz} Systematic	T_{20} Systematic
Polarization	6.0%	6.0%
Dilution factor	6.0%	2.5%
Packing fraction	3.0%	3.0%
Trigger/Tracking Eff.	1.0%	1.0%
Acceptance	0.5%	0.5%
Charge Determination	1.0%	1.0%
Detector resolution and efficiency	1.0%	1.0%
Total	9.2%	7.4%

Table 5: Estimates of the scale dependent contributions to the systematic error of A_{zz} and T_{20} .

The other uncertainties in Table 5 are very standard contributions which are difficult to reduce beyond the listed instrumental lower limit.

3.4.2.1 Time Dependent Factors

Eq. 26 involves the ratio of counts, which leads to cancellation of several first order systematic effects. However, the fact that the two data sets will not be taken simultaneously leads to a sensitivity to time dependent variations which will need to be carefully monitored and suppressed when possible. To investigate the systematic differences in the time dependent components of the integrated counts, the effects from calibration, efficiency, acceptance, and luminosity between the two polarization states must be considered. In order to look at the effect on A_{zz} due to drifts in beam current measurement calibration and detector efficiency, Eq. 26 is rewritten explicitly in terms of the raw measured counts N_1 and N ,

$$\begin{aligned}
A_{zz} &= \frac{2}{fP_{zz}} \left(\frac{N_1^c}{N^c} - 1 \right) \\
&= \frac{2}{fP_{zz}} \left(\frac{Q\varepsilon l\mathcal{A}}{Q_1\varepsilon_1 l\mathcal{A}} \frac{N_1}{N} - 1 \right)
\end{aligned} \tag{28}$$

where Q represents the accumulated charge, and ε is the detector efficiency. The target length l and acceptance \mathcal{A} are identical in both states, to first order.

We can then express Q_1 as the change in beam current measurement calibration that occurs in the time it takes to collect data in one polarization state before switching such that $Q_1 = Q(1 - \delta Q)$. In this notation, δQ is a dimensionless ratio of charges in the different polarization states. A similar representation is used for drifts in detector efficiency leading to,

$$A_{zz} = \frac{2}{fP_{zz}} \left(\frac{N_1 Q (1 - \delta Q) \varepsilon (1 - \delta \varepsilon)}{N Q \varepsilon} - 1 \right), \tag{29}$$

which leads to,

$$A_{zz} = \frac{2}{fP_{zz}} \left(\frac{N_1}{N} (1 - \delta Q - \delta \varepsilon + \delta Q \delta \varepsilon) - 1 \right). \tag{30}$$

Estimates of δQ and $\delta\varepsilon$ can be obtained from previous experiments. For the HRS detector drift during the JLab transversity experiment E06-010, the detector response was measured such that the normalized yield for the same condition over a three month period indicated little change ($< 1\%$). These measurements indicated that for the short time (20 minutes) between target spin flips, the detector drift should be less than 1% times the ratio of the time period between target spin flips and three months. Also considering the period between target polarization states to be ≈ 12 hours leading to an overall drift $\delta\varepsilon \sim 0.01\%$. A similar approach can be used to establish an estimate for δQ using studies from the g2p/GEp experiment, resulting in $\delta Q \sim 0.01\%$. The SANE experiment with a beam current of 100 nA also provides some information. In this case, the relative stability of the current monitors is on the order of 1×10^{-3} , showing oscillations with a period of about an hour.

Expressing A_{zz} in terms of the estimated experimental drifts in efficiency and current measurement,

$$A_{zz} = \frac{2}{fP_{zz}} \left(\frac{N_1}{N} - 1 \right) \pm \frac{2}{fP_{zz}} \delta\xi. \quad (31)$$

where $\delta\xi = \delta Q + \delta\varepsilon$. This leads to a contribution to A_{zz} on the order of 1×10^{-3} ,

$$dA_{zz}^{drift} = \pm \frac{2}{fP_{zz}} \delta\xi = \pm 3.7 \times 10^{-3}. \quad (32)$$

Using the standard dilution factor and classically accessible polarization, the precision required in the raw A_{zz} measurement for already-approved DIS b_1 experiment is

$$\delta A_{zz}^{raw} = \frac{fP_{zz}}{2} \delta A_{zz} = 1.5 \times 10^{-4}. \quad (33)$$

For this proposed A_{zz} measurement, f is changing with x significantly. For $x \sim 1$ the dilution is greater ($f \sim 0.5$) than for the larger x ($f \sim 0.1$), where the large signal size indicated by A_{zz} model calculations requires considerably less precision. The critical point is $x \sim 0.8$ where f is less than 0.2 such that

$$\delta A_{zz}^{raw} = \frac{fP_{zz}}{2} \delta A_{zz} = \frac{(0.19)(0.2)}{2} (0.05) = 1.0 \times 10^{-3}. \quad (34)$$

So even this most sensitive point is still around an order of magnitude less constrained than the b_1 measurement.

Detector efficiencies can drift for a variety of reasons, including fluctuations in gas quality, high voltage drift, or drifts in the spectrometer magnetic fields. All of these types of variation can be controlled and minimized during the experiment through careful monitoring as well as systematic studies of the data collected. The identical configuration of the two polarization states minimizes the relative changes in luminosity with respect to time. Consistency checks on the measured cross section data can be implemented to ensure the quality of each run used in the asymmetry analysis. Fluctuations in luminosity due to target density variation can be kept to a minimum by keeping the material beads at the same temperature for both polarization states through control of the microwave and the liquid helium (LHe) evaporation. The helium vapor

pressure reading provides an accuracy of material temperature changes at the level of $\sim 0.1\%$. Beam rastering can also be controlled to a high degree.

The dominant source of any variation in acceptance \mathcal{A} from state to state will be the stability of the target magnetic field. The capacity to set and hold the target superconducting magnet to a desired holding field is $\delta B/B = 0.01\%$. The same target cup will be used for each state, which removes any variation in the target length l .

3.4.2.2 Drift Mitigation

Uncertainty in the measuring devices (or resulting normalization deviations) must be small compared to the scale of the asymmetry at the helicity reversal frequency. The beam noise that can contribute to these normalization deviations comes from beam current, beam position, beam energy, beam size (consistent rastering), and beam halo. Detectors drifts in photomultiplier tube (PMT) gain can change the number of events above a discriminator threshold, which can become critical when the device PMT behavior changes significantly between helicity states. This is also true for drift chamber efficiency, spectrometer analyzing field, atmospheric pressure and temperature all affect these systems. The target's superconducting magnet will be operated in persistent current mode, which provides a field uniformity of better than 10^{-4} [55]. The NMR resonance frequency can also be used to monitor the field with an accuracy exceeding 10^{-5} .

The most obvious way to improve the experiment considering these contributions is to increase the helicity flip frequency. Probably the most practiced way to do this is to use two different target cells alternating the cell position between a polarized target cell and an unpolarized target cell. By doing this additional uncertainties from using different packing fractions, effective target densities, and target nuclear-chemical compositions are introduced that would not be present when using identical targets for each helicity state. These contributions may be able to be mitigated by alternating which cell is polarized. It is possible to polarize a particular cell without being in beam having it outside the homogeneous portion of the target field (beam line). In this way a target cell helicity can be prepared while taking data on the other cell. This could potential allow multiple helicity changes in a 24 hour period.

In addition to greater frequency in helicity changes, the initial polarization build-up can also be enhanced. It is possible to install an electrically controlled microwave attenuator which will allow a larger amount of microwave power to dump into the target material to speed up polarization. The attenuator can then be adjusted to the required power to sustain polarization with the addition of the electron beam.

The uncertainty estimate in charge that results in a small absolute change in the observable is described in the proposal in the Section 3.4.2.1. Analytically there is a component of uncertainty that propagates with the other relative errors and only a very small piece that results in a drift in the observable. The resulting expression for the charge and other contributions to the drift in the observable is expressed as,

$$\delta A_{zz}^d = \pm \frac{2}{fP_{zz}} \delta \xi, \quad (35)$$

where $\delta \xi$ contains the sum of δQ , $\delta \epsilon$, δl , and δA . This means that to accurately represent δA_{zz}^d we must obtain only the residual deviation from the two polarization states in the time span of a single

cycle (sampling of that data point). The value used for δQ is an estimate based on the actual effect seen in an observable which helps us to separate the relative contribution from the drift in a given time frame.

3.4.2.3 Trigger-Tracking For the most part, an easy way to determine whether or not drift will lead to an effect on the error is to determine if the change over time is seen in one polarization state and not the other with respect to the observable. Effects from trigger, cuts, and tracking efficiency do lead to errors in normalization, however both polarization states see the same stochastic fluctuation over the course of a cycle leading only to a small relative uncertainty in the observable. Aspects of the error that are non-stochastic and follow an unknown trend have been estimated in the proposal under the name ‘detector drifts.’ A secondary estimate was obtained based on HRS detector stability using Hall A transversity data for detected pions. The resulting drift was 2.2×10^{-4} . The detector thresholds will be set conservatively while using meticulous on-line monitoring and checks to the relative changes in tracking efficiency between slugs. For our present estimate including trigger, tracking, cuts, and detector errors that show up strictly as contributions to $\delta\xi$, we estimate no larger than 2.2×10^{-4} .

3.4.2.4 Target Dilution and Length There are presently UVA designs for target cup and material fabrication to minimize the probability of changes to target dilution in the form of material loss over time. The cup contains multiple hole arrays that are only a 0.1 mm in size. The material shape and consistency is optimized to maximize the packing fraction and minimize the fracturing capacity. The ammonia is hand selected to reduce the structural faults to obtain beads approximately 2 mm in diameter which have already undergone multiple steps of mechanical stress including being pre-irradiated at NIST with a $10 \mu\text{A}$ beam. The temperature and thus the density of the target is kept the same in both polarized and unpolarized states. There are four temperature sensors in a standard solid polarized target setup that can be used to monitor this. The temperature is controlled via LHe evaporation, microwave, and beam heating. All three are used to maintain consistent temperature in both polarization states.

The polarized material to be used in the experiment will be contained in 3 cm long, 2.54 cm diameter cylinder cups with their axes parallel to the beam. The cylinders fit inside the 4 cm diameter vertical cylindrical tail piece at the bottom of the refrigerator. The tail piece is full of liquid helium to about 20 cm above the beam level. The heat and radiation of the beam is distributed uniformly over the cross section of the target normal to the incident beam by a combination of slow and fast rasters. The fast raster normally is a 2mm by 2mm square shape, traced by the sub-millimeter beam at kHz rates. The slow raster normally is a 1 cm maximum radius spiral, traced at constant tangential speed, covering the rastered area with 5% dose uniformity at 30 Hz and can be synchronized to the usual helicity flip signals [56].

The averaging of the target length done by the rasters results in an effective length that is determined by the fraction of the cup volume (equivalently, the rastered volume) that is filled with ammonia [56]. A possible change in the effective target length between the polarized and unpolarized periods of a measurement cycle could come from a net change of material in the raster volume, for instance if an ammonia bead was shaken out of the sample. Since the raster diameter is

25% smaller than the cup diameter, there will always be material above the raster region that would shift into the missing bead's place in the an unlikely event of material loss within the rastered region. A possible estimate of the length change can be obtained by considering the ratio of the 0.008 cm^3 volume of a fragment to the 6.8 cm^3 raster volume (including packing fraction) the ratio is $\sim 1/850$.

The only documented instance with ammonia polarized targets and CEBAF $\sim 100 \text{ nA}$ beams of a possible rearrangement of material about the target NMR coil that might indicate an associated net change in material was seen during E07-003 (SANE) which took about 500 hours of $\geq 85 \text{ nA}$ beam. During one 20 h polarized and unpolarized cycle, the loss of 1 or 2 fragments would result in a $\sim 1 \times 10^{-3}$ change in target length, with a $\sim 20\text{h}/500\text{h}$ probability. No instances of material fragmentation, which could potentially lead to net losses in the raster region have been observed with up to 150 nA CW CEBAF beams (E93-026, E01-006, E07-003). In addition, any rearrangement of material would be immediately recognized by a change in the NMR signal, which can be used to ensure that no loss of a target fragments occurred between cycles. In the rare event that this does occur, only a single target cycle would be affected and the data can be recovered after being separated at the point of the event.

The only instances of material fragmentation for ammonia targets were observed at SLAC, in the E143/E155/E155x series of experiments, but the SLAC beam is pulsed, with 300 ns wide pulses of $\sim 2 \text{ mA}$ current at 119 Hz repetition rate [57]. Such beam time structure can be expected to damage the ammonia crystals by thermal shock. In fact, to further prevent possible shock effects at JLab, the polarized target experiments in Hall C implemented the procedure of gradual ramping up of the beam current after beam trips.

All changes to the material that occur during movement of the target ladder or annealing can only happen at the end of each pair of measurement cycles and are irrelevant for the preceding or following cycles. Small changes to material NMR loop coupling are consistent to both polarization states and exist as a relative error in the polarization.

Depolarization using LHe is a relatively standard technique. In this procedure, the beam is turned off and the LHe fill valve that controls the LHe level that surrounds the target insert is slowly reduced as to not replenish the LHe evaporation until the material has warmed up and the polarization has died out. The LHe is gradually filled again as in the standard evaporation mode and again set on automated control. Once the material is unpolarized and again submerged under the LHe the microwaves are turned on in off-resonance mode. The unpolarized target is then ready for beam. This procedure provides a quick way to kill polarization while returning the unpolarized state to the exact condition of the polarized state. The small fluctuation in density, temperature and NMR material couple occur in both states and are a small relative error in the polarization. All other aspects that may result in addition to the drift are negligible.

For example, the target operating temperature is $\sim 1.1 \pm 0.15 \text{ K}$, well below the superfluid point. Over that range, the LHe density, changes by 4×10^{-5} (the density actually increases below $\simeq 1.1 \text{ K}$ and increases above, by about equal amounts over the temperature interval [58]). The lattice constant of deuterioammonia [59] changes from 5.048 \AA at 2 K to 5.073 \AA at 77 K , corresponding to a 1×10^{-5} change over the $\pm 0.15 \text{ K}$ interval considered above. For a 60% packing fraction, the change would be 2.3×10^{-5} for a 0.15 K unexpected temperature difference between

polarization states. Any possible unaccounted changes in target length between the polarized and unpolarized parts of each cycle can also be monitored by recording the time dependence of the luminosity with a $\simeq 0.5 \times 10^{-4}$ accuracy.

3.4.2.5 Solid Angle

The error that arises in the observable due to beam position and magnet currents over time is inherently very difficult to separate into drift and relative uncertainty. The 0.1% error over a 12 hour period is probably quite accurate, however, being that both polarization states experience the same fluctuations its likely that the majority of the uncertainty is relative. There are also concerns on acceptance due to beam position drift. Beam drift will be monitored during the experiment and accounted for during analysis. The largest part of this uncertainty is also a relative contribution to both target states. The contribution to the drift can be minimized with the feedback system built for parity experiments .

Trends that arise from dependence of yield on magnet currents in detectors are a concern related to the spectrometer acceptance. The drift effect can be made to be small, for the HRS typically less than 10^{-4} for the dipole and 10^{-3} for the three quads, and similarly for the HMS. The effects on the acceptance can be determined and corrected through careful analysis. Naturally, the target magnet current does not need to be changed between cycles, as the uniformity, stability, and setability pointed out in the proposal eliminate field variation between the two polarization states. The residual drift from solid angle effects after such correction is expected to be no larger than 0.01%. This value was already accounted for in Section 3.4.2.3.

3.4.2.6 Beam Current Monitors

Information has been extracted from experiment E06-010 for high current (10-15 μA), in which all the systematics are included in the yield studies including detector drift, acceptance drift, BCM drift and acceptance due to BPM drift. The beam charge asymmetries between two helicity states using the luminosity monitors for experiment E06-010 has been shown to be at the level of 4×10^{-5} with a width of 2.3×10^{-4} . An additional estimate on the change in the BCM calibration constant is seen in experiment E08-027 resulting in a absolute deviation of 2.0×10^{-4} over the course of six days. Long term drifts can be reduced by careful thermal isolation of the BCMs, however resulting trends will be need to be studied and corrections implemented.

Fluctuations in the calibration of beam current measuring devices can be well understood and mitigated. Even when calibrations are taken frequently, a small change in the BCM response over the course of a single helicity flip iteration can contribute a drift on the order of 1×10^{-4} . A Boosted Decision Tree regression maybe used similar to that used for the temperature dependence of the Q-meter. This would require accurate temperature monitoring of the BCM stainless steel pillbox resonant cavity in operation. Creating a heat regulating system using a fluid circulated chiller could help to both stabilize and accurately measure the temperature. Additional temperature stabilization of analog cables, and optimizing cable length maybe also help.

3.4.2.7 Systematic Summary

It is essential to consider each uncertainty and each source separately as well as understand systemic coupling. This proposed A_{zz} measurement would be a great benefit to understand and minimize systematic uncertainties for small asymmetry measurements such as b_1 . Having data at a large range of beam current, energy, and target types while studying beam noise and detector stability can help to build a comprehensive map of critical systematic issues. Other systematic minimization techniques can be explored during A_{zz} in addition to the systematic minimization mentioned in this proposal, which will be critical for b_1 [60] and could help many other future experiments. In fact there is no better experimental opportunity to study the systematics of probing asymmetries in Hall C than A_{zz} at high x . Because of the scale of the predicted asymmetry A_{zz} for large x , the drifts that can corrupt b_1 are only relevant for the lower x points, although for A_{zz} in this region a systematic error of the order of (1×10^{-3}) would be very good, which has an order of magnitude more leeway than for b_1 .

3.5 Polarized Target

This experiment will use the JLab/UVa dynamically polarized solid ND_3 target operated in longitudinal mode. The target is typically operated with a specialized slow raster and beamline instrumentation capable of characterizing the low current 50-100 nA beam. All of these requirements have been met previously in Hall C. The polarized target (see Fig. 18), has been successfully used in experiments E143, E155, and E155x at SLAC, and E93-026, E01-006 and E07-003, E08-027 and E08-007 at JLab. A similar target was used in Hall B for the EG1, EG4, and DVCS experiments.

The JLab/UVa target underwent significant renovation and improvement during the recent g2p run [61]. The magnet was replaced early in the run, and the target then performed consistently. A new 1 K refrigerator and target insert were designed and constructed by the JLab target group. The cryogenic pumping system has been overhauled. In particular, the older Alcatel 2060H rotary vane pumps have been replaced with new Pfeiffer DU065 magnetically coupled rotary vane pumps, and the pump controls were refurbished. The target motion system has been rebuilt from scratch.

The target operates on the principle of Dynamic Nuclear Polarization, to enhance the low temperature (1 K), high magnetic field (5 T) polarization of solid materials by microwave pumping. The polarized target assembly contains several target cells of 3.0 cm length that can be selected individually by remote control to be located in the uniform field region of a superconducting Helmholtz pair. The permeable target cells are immersed in a vessel filled with liquid Helium and maintained at 1 K by use of a high power evaporation refrigerator. The coils have a 50° conical shaped aperture along the beam axis which allow for unobstructed forward scattering.

The target material is exposed to microwaves to drive the hyperfine transition which aligns the nucleon spins. The heating of the target by the beam causes a drop of a few percent in the polarization, and the polarization slowly decreases with time due to radiation damage. Most of the radiation damage can be repaired by periodically annealing the target, until the accumulated dose reached is greater than about $0.5 \times 10^{17} e^-/\text{cm}^2$, at which time the target material needs to be replaced.

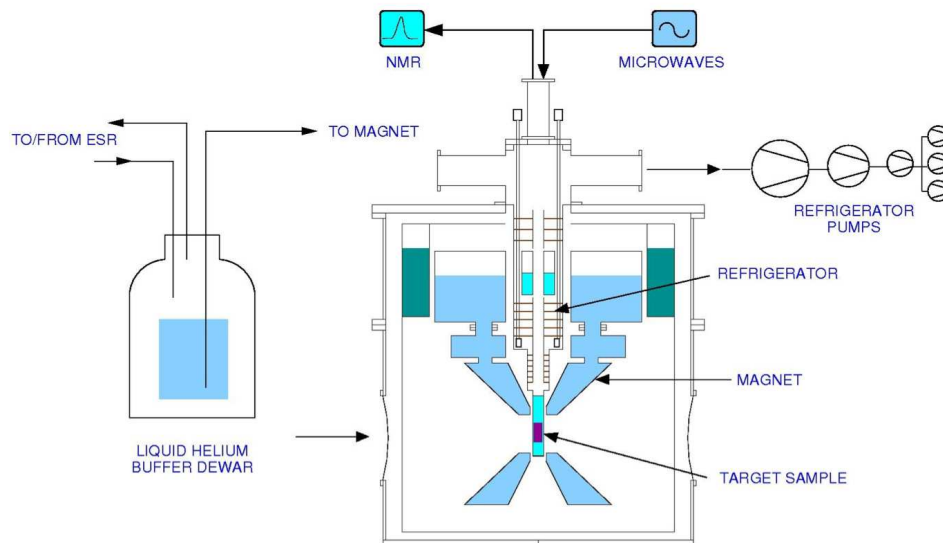


Figure 18: Cross section view of the JLab/UVA polarized target. The proposed experiment will use the modified Hall B magnet, where the backwards-scattering cone is blocked with quench protection circuitry. Figure courtesy of C. Keith.

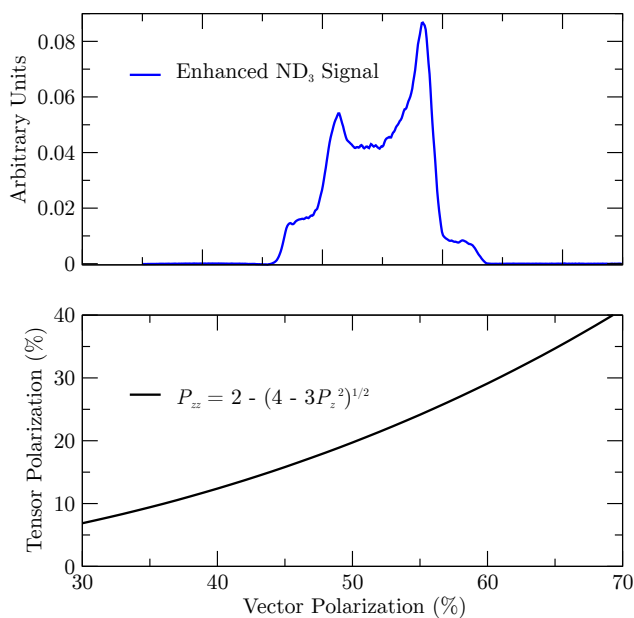


Figure 19: **Top:** NMR signal for ND_3 with a vector polarization of approximately 50% from the GEN experiment. **Bottom:** Relationship between vector (P_z) and tensor (P_{zz}) polarization in equilibrium, and neglecting the small quadrupole interaction.

3.5.1 Polarization Analysis

The three Zeeman sublevels of the deuteron system ($m = -1, 0, 1$) are shifted unevenly due to the quadrupole interaction [62]. This shift depends on the angle between the magnetic field and the electrical field gradient, and gives rise to two separate transition energies. Hence, the unique double peaked response displayed in Fig. 19. When the system is at thermal equilibrium with the solid lattice, the deuteron polarization is known from:

$$P_z = \frac{4 + \tanh \frac{\mu B}{2kT}}{3 + \tanh^2 \frac{\mu B}{2kT}} \quad (36)$$

where μ is the magnetic moment and k is Boltzmann's constant. The above equation is valid for polarizations with the magnetic sublevels distributed in a Boltzmann distribution. The vector polarization can be determined by comparing the enhanced signal with that of the TE signal (which has known polarization). This polarimetry method is typically reliable to about 3.9% relative.

Similarly, the tensor polarization is given by:

$$P_{zz} = \frac{4 + \tanh^2 \frac{\mu B}{2kT}}{3 + \tanh^2 \frac{\mu B}{2kT}} \quad (37)$$

From Eqs. 36 and 37, we find

$$P_{zz} = 2 - \sqrt{4 - 3P_z^2} \quad (38)$$

In addition to the TE method, polarizations can be determined by analyzing NMR lineshapes as described in [63] with a typical 7% relative uncertainty. At high polarizations, the intensities of the two transitions differ, and the NMR signal shows an asymmetry R in the value of the two peaks, as shown in Fig. 19. The vector polarization is then given by:

$$P_z = \frac{R^2 - 1}{R^2 + R + 1} \quad (39)$$

and the tensor polarization is given by:

$$P_{zz} = \frac{R^2 - 2R + 1}{R^2 + R + 1} \quad (40)$$

This measuring technique can be used as a compliment to the TE method resulting in reduced uncertainty in polarization.

3.5.2 Elastic Normalization of Tensor Polarization

Along with the aforementioned techniques to determine the target polarization, we will also make use of previous, high precision elastic scattering asymmetry measurements. In particular, NIKHEF created a tensor deuteron target with an atomic beam source and were able to measure the polarization of the gas with both a Briet-Rabi polarimeter as well as an ion-extraction polarimeter [64, 65]. By measuring in very similar kinematics as NIKHEF, we will be able to normalize our absolute tensor polarization to the NIKHEF result. This is not only beneficial for this experiment, but also the deep inelastic experiment that has been conditionally approved [47].

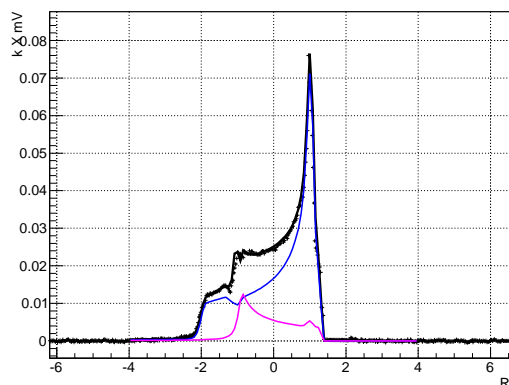


Figure 20: A preliminary result showing the NMR signal of deuterated butanol with a tensor polarization enhanced from 20% to just over 30% after applying the selective saturation technique mentioned.

3.5.3 Tensor Polarization Enhancement

To achieve the highest FOM for the spin-1 alignment scattering experiments, it is necessary to maximize the tensor polarization of the solid-state targets throughout the beam target interaction time. Optimization of the spin-1 alignment in the target ensemble can be achieved by applying RF irradiation at select frequencies with the required RF coil power generated. The RF manipulated lineshape based on the numerical solutions to the solid-effect rate equations can be used to understand the spin-dynamics over the frequency domain of the deuteron NMR signal. Optimization is achieved using a critical RF fundamental decay constant which partially saturates the overlapping regions of the Pake doublet corresponding to negative tensor polarization for a given frequency. Enhancement results from reducing the negative contributions to the tensor polarization of the sample and increasing the positive contributions at the same polar angle, θ , (with respect to molecular orientation with the magnetic field). The RF manipulation of the population of the $m = 0$ magnetic substate is observed in the NMR signal as an increase in the intensity of one transition and a decrease in the other at the same θ .

Studies are in progress using deuterated butanol (C_4D_9OD), which was chosen for its ease of paramagnetic center optimization and its similar lineshape to ND_3 . A preliminary result is shown in Fig. 20 for a deuterated butanol polarized during a UVA cooldown. Prior to RF-manipulation the sample was vector polarized to just over 50%. The selective semi-saturation technique was applied to the smaller peak while the pedestal was saturated with RF. A tensor polarization of just over 30% was measured using line fitting, which relies on the numerical solutions to the solid-effect rate equations in only the peak positions [66, 67, 68, 69].

Optimization of the paramagnetic centers of ND_3 is more complex than for butanol requiring both warm and cold irradiation. Even under ideal center concentration, ND_3 will likely not perform as well as deuterated butanol simply because it will not polarized to over 50% at 5 T. Paramagnetic center optimization using cold irradiation and sensitivity to field strength is still very much under investigation. It is anticipated that additional enhancement for ND_3 will be required by rotation of

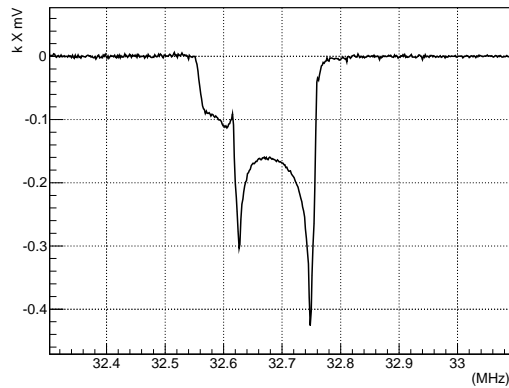


Figure 21: The deuterium magnetic resonance line shape showing the recent achievement of high tensor polarization of deuterated butanol after RF saturation of a pedestal at the UVA polarized target lab accomplished during their April 2014 cool-down.

sample during selective semi-saturation, which is also currently in active development [70].

The studies also indicate that microwaves used during DNP do not interfere with the saturation from the RF irradiation when sufficient power is used. This implies that RF over the pedestal can be done the same time DNP is performed to enhance the area while taking beam in an experiment.

Negative polarization can be achieved but can not be held in place at 1 K. For electron beam experiments that can run at very low current ($< 1\text{nA}$) a dilution fridge can be used to keep the tensor enhancement in a frozen spin state. Clearly this is not practical for our demand of beam current. Negative polarization of course is also possible for photon beam experiments where the Kapitza resistance is not really an issue compared to charge beams.

Research and development is ongoing to study various techniques to increase the target's figure of merit. In addition to the above hole burning and semi-saturation that are currently being researched at UVA [52, 53, 54, 60], there are further options to develop increased tensor polarization by operating at higher target magnetic fields [71], to optimize the pre-irradiation dose on the target material [72], and to increase luminosity by building an extended target or a target with multiple cells [73].

3.5.4 Depolarizing the Target

To move from polarized to unpolarized measurements, the target polarization will be annihilated using destructive RF. A single higher powered ($\sim 100\text{ mW}$) RF sweep passed through the coil used to manipulate the alignment can reduce total target polarization to less than half in a couple of milliseconds. Microwaves can stay on when set off resonance while the RF coil can achieve total depolarization in just a few seconds.

During unpolarized data taking the incident electron beam heating is enough to remove the thermal equilibrium polarization.

We are able to verify that the target is in the unpolarized state via NMR measurements. The

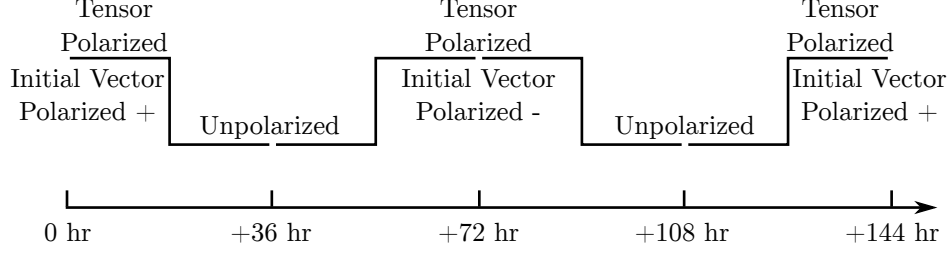


Figure 22: A visual demonstration of the 72 hour polarization cycle that will be used to reduce time-dependent systematic effects. For the lower Q^2 measurements, the cycle will happen over 12 and 18 hour periods. The initial vector polarization before tensor enhancement will be flipped at every re-polarization to reduce systematics.

target material will be kept at 1 K for polarized and unpolarized data collection, and the target field will be held constant for both states as well. These consistencies are used to minimize the systematic differences in the polarized and unpolarized data collection. To minimize systematic effects over time, the polarization condition will be switched twice in a 72 hour period, as shown in Fig. 22. This will be sufficient to account for drift in integrated charge accumulation. Additionally, upon repolarization the direction of the initial vector polarization will be flipped to reduce systematic effects. As shown in Eq. 38, positive tensor polarization can be gained from either a positive or negative initial vector polarization. Unfortunately, this method only works well for positive tensor polarization, and current attempts at enhancement of negative P_{zz} through DNP indicate that it cannot be maintained while in the electron beam.

3.5.5 Dilution Factor

To derive the dilution factor, we first start with the ratio of polarized to unpolarized counts. In each case, the number of counts that are actually measured, neglecting the small contributions of the thin aluminium cup window materials, NMR coils, etc., are

$$N_1 = Q_1 \varepsilon_1 \mathcal{A}_1 l_1 [(\sigma_N + 3\sigma_1)p_f + \sigma_{He}(1 - p_f)], \quad (41)$$

and

$$N = Q \varepsilon \mathcal{A} l [(\sigma_N + 3\sigma)p_f + \sigma_{He}(1 - p_f)]. \quad (42)$$

where Q represents accumulated charge, ε is the detector efficiency, \mathcal{A} the cup acceptance, and l the cup length.

For this calculation we assume similar charge accumulation such that $Q \simeq Q_1$, and that the efficiencies stay constant, in which case all factors drop out of the ratio leading to

$$\begin{aligned} \frac{N_1}{N} &= \frac{(\sigma_N + 3\sigma_1)p_f + \sigma_{He}(1 - p_f)}{(\sigma_N + 3\sigma)p_f + \sigma_{He}(1 - p_f)} \\ &= \frac{(\sigma_N + 3\sigma(1 + A_{zz}P_{zz}/2))p_f + \sigma_{He}(1 - p_f)}{(\sigma_N + 3\sigma)p_f + \sigma_{He}(1 - p_f)} \end{aligned}$$

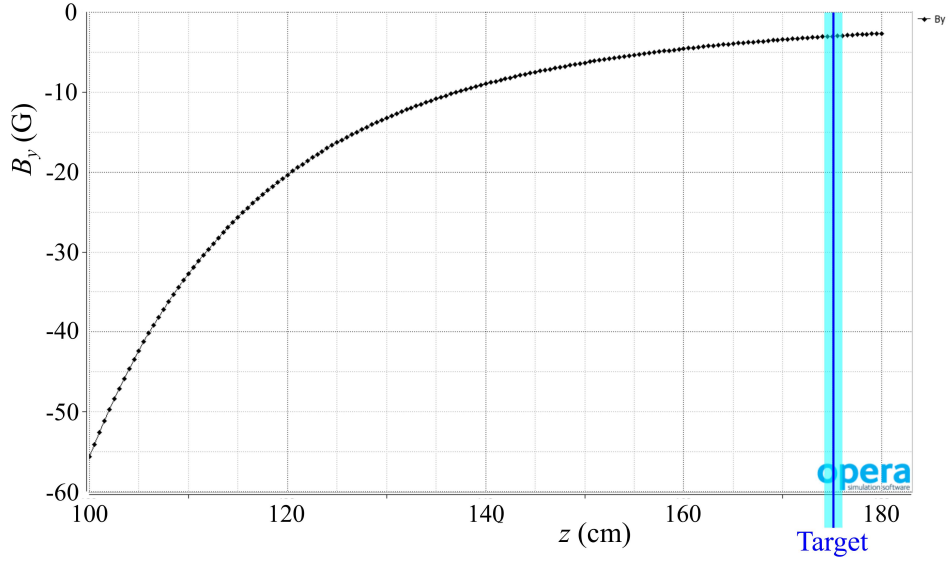


Figure 23: TOSCA calculations [49] indicated that the fringe fields of the SHMS Horizontal Bender magnet will have a negligible effect on the target.

$$\begin{aligned}
 &= \frac{[(\sigma_N + 3\sigma)p_f + \sigma_{He}(1 - p_f)] + 3\sigma A_{zz}P_{zz}/2}{(\sigma_N + 3\sigma)p_f + \sigma_{He}(1 - p_f)} \\
 &= 1 + \frac{3\sigma A_{zz}P_{zz}/2}{(\sigma_N + 3\sigma)p_f + \sigma_{He}(1 - p_f)} \\
 &= 1 + \frac{1}{2}f A_{zz}P_{zz}, \tag{43}
 \end{aligned}$$

where $\sigma_1 = \sigma(1 + A_{zz}P_{zz}/2)$ has been substituted, per Eq. 8, with $P_B = 0$. It can be seen that the above result corresponds to Eq. 11.

3.5.6 Target and Horizontal Bender Magnets

Although it was noted that the SHMS Horizontal Bender (HB) magnet is expected to have significant fringe fields [49], we expect this to have a minimal effect on the DNP target. The center of the target will be located approximately 1.75 m away from the 3 T HB where TOSCA calculations indicate that the fringe fields will be < 5 G and have a gradient of ~ 0.2 G/cm, as shown in Fig. 23. The maximum effect this would have on the target material is 12ppm, which is well within the required 100ppm target field uniformity required.

Additionally, we don't expect a coupling between the HB fringe fields and the DNP magnet to cause an issue. The Hall A g2p experiment (E08-027) used the same target alongside a similar 1.5 T septa magnet that was placed 1.58 m from the center of the target. During the course of running, the septa suffered a catastrophic failure during which the magnetic field stability, measured by the central frequency of the proton NMR peak, was maintained at < 100 ppm as shown in Fig. 24. Additionally, the TOSCA study performed prior to the g2p experiment agreed very well with

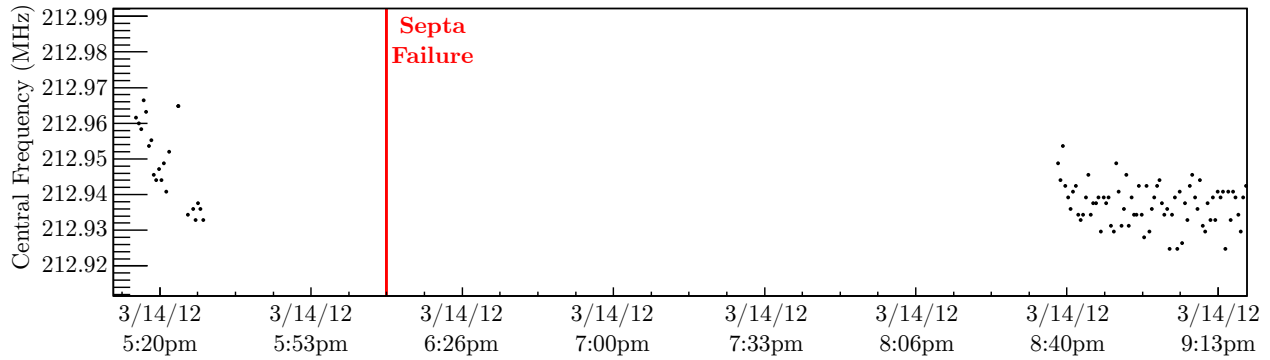


Figure 24: Even during a catastrophic failure of the septa magnet during the Hall A g2p experiment, the DNP target maintained a < 100 ppm stability. This configuration was very similar to the proposed experiment where the DNP target will be placed near the SHMS horizontal bender magnet.

field mapping, which also indicated that the septa would have a negligible coupling on the target magnet [74].

3.6 Overhead

Table 6 summarizes the expected overhead during beam, which sums to 11 days. The dominant overhead comes from switching from the polarized to unpolarized state and vice versa, and target anneals. The target will need to be annealed about every other day, and the material replaced once a week. Measurements of the dilution from the unpolarized materials contained in the target, and of the packing fraction due to the granular composition of the target material will be performed with a carbon target.

We also note that this experiment will use the JLab/UVA DNP target, as well as additional temperature monitors and controls on the BCMS, which will require significant lead time without beam for installation. To reduce decommissioning time, this experiment can run immediately before the b_1 experiment (E12-13-011) that requires identical equipment.

4 Previous PAC Comments and Concerns

In this section we summarize the comments and concerns that were raised by the PAC42 committees on letter of intent LOI12-14-002 and the PAC43 committees on the C2 conditionally-approved proposal PR12-15-005.

4.1 PAC42 Theory Advisory Committee

“This Letter of Intent describes a measurement of the tensor-polarized asymmetry A_{zz} in electron scattering on polarized deuterium in the quasi-elastic region, at values of $x = 0.8 - 1.75$ (x is the equivalent Bjorken variable at the nucleon level) and

Overhead	Number	Time Per (hr)	(hr)
Polarization/depolarization	38	2.0	76.0
Target anneal	15	4.0	60.0
Target T.E. measurement	6	4.0	24.0
Target material change	4	4.0	16.0
Packing Fraction/Dilution runs	20	1.0	20.0
BCM calibration	9	2.0	18.0
Optics	3	4.0	12.0
Linac change	2	8.0	16.0
Momentum/angle change	3	2.0	6.0
			11 days

Table 6: Major contributions to the overhead.

$Q^2 = 12 \text{ GeV}^2$. The aim is to determine with this observable the S/D wave ratio in the deuteron wave function at large relative momenta $k > 300 \text{ MeV}$, which is important for understanding the NN interaction at short distances and the properties of the dominant pn short-range correlations in heavier nuclei. The same tensor-polarized asymmetry was/will be measured in elastic scattering (deuteron form factor) and deep-inelastic scattering (structure function b_1); the proposed measurement in quasi-elastic scattering would fill the gap and study this observable in the region where it is most directly related to the short-range NN interaction. The tensor asymmetry at large recoil momenta also serves as a sensitive test of “relativistic effects” in the treatment of deuteron structure, which are an important aspect of the overall theoretical framework and the object of ongoing studies. A unique feature of the measurement proposed here is that it selects small-size configurations in the deuteron both through the tensor asymmetry (D -state) and the choice of kinematics ($x > 1$), amplifying the overall effect. The use of $x > 1$ for selecting small-size NN configurations has been demonstrated in previous studies of deep-inelastic structure.

The measurement proposed here arises from a well-developed context, presents a clear objective, and enjoys strong theory support. It would further explore the nature of short-range pn correlations in nuclei, the discovery of which has been one of the most important results of the JLab 6 GeV nuclear program. Development of a full proposal should be encouraged.”

4.2 PAC43 Theory Advisory Committee

“The authors propose to measure the tensor-polarized asymmetry A_{zz} in inclusive electron scattering on polarized deuterium in the quasi-elastic region with Bjorken x_B in the range $0.3 < x_B < 2.0$ and momentum transfer Q^2 varying in $0.2 (\text{GeV}/c)^2 < Q^2 < 2.9 (\text{GeV}/c)^2$. In a plane-wave picture of the scattering process, this observable

is sensitive to the ratio of the D- to S-component in the deuteron wave function, and the proposed kinematic conditions are such that large relative momenta $k > 300$ MeV in these components would be probed. This is important for understanding the nucleon-nucleon (NN) interaction at short distances and the properties of the dominant pn correlations in heavier nuclei. The same tensor polarized asymmetry has been/will be measured in elastic deuteron scattering (the T_{20} observable) and deep-inelastic scattering (the b_1 structure function): the proposed measurements in quasi-elastic kinematics would fill the gap and study the A_{zz} asymmetry in the region where it is most directly related to the short-range NN interaction. The tensor asymmetry at large recoil momenta also provides a sensitive test of relativistic effects in the treatment of deuteron structure as well as final-state interactions (FSI) in the outgoing pn pair, both of which are important aspects of the overall phenomenological framework and the object of ongoing studies by a number of theorists (some of whom are listed as co-authors of the present proposal). Indeed, preliminary results for A_{zz} in kinematics relevant to this proposal are presented corresponding to a variety of different models for the treatment of the above effects and different input deuteron wave functions. Drastically different predictions are obtained depending on whether off-shell effects are included in FSI.

The authors of the proposal also plan to measure the tensor polarization in elastic scattering at four Q^2 values in the range $0.2 \text{ (GeV}/c)^2 < Q^2 < 1.8 \text{ (GeV}/c)^2$, the additional planned measurement at $Q^2 = 0.2 \text{ (GeV}/c)^2$ being for calibration purposes only. These measurements would complement and corroborate existing ones (projected errors at the proposed Q^2 are similar to those of already available data).

The experiment proposed here arises from a well-developed context, presents a clear objective, and enjoys strong theory support. It would further explore the nature of pn correlations in nuclei, the discovery of which has been one of the most important results of the JLab 6 GeV program.”

4.3 PAC42 Technical Advisory Committee

“This experiment utilizes the same apparatus and techniques as the conditionally approved b1 experiment C13-12-011. The comments in the TAC report for that experiment also apply to this experiment.

The requirement to understand and mitigate time-dependent systematic effects may be less as the asymmetry A_{zz} , at least for $x > 1$, is expected to be larger than for b1. However, measuring with $\delta A_{zz} < 0.10$ still requires a systematic control of the raw asymmetry to better than 1%. This is still challenging with a target polarization that is cycled on and off about once a day. Furthermore, at $x > 1$, short range structure enhances inclusive cross sections in nuclei relative to deuterium. This will reduce the dilution factor for $x > 1$ measurements, reducing the raw asymmetries to levels where understanding and controlling systematic errors will still be important.”

4.4 PAC43 Technical Advisory Committee

- “ 1. Significant laboratory engineering and technical resources will be required for the JLab Hall B/UVA polarized ND₃ target (A.K.A. the “g2p longitudinally Polarized Target”)
2. As with C12-13-011 (“b1”), this experiment relies on the tensor polarization of the ND₃ target. C12-13-11 was conditionally approved (C1) in PAC40, and dependent on demonstrating “that a tensor polarization of at least 30% be achieved and reliably demonstrated under experimental conditions.” [from PAC40 Final Report, p 19]
 - (a) The “RF hole burning” technique used to enhance the tensor polarization removes the ability to extract the tensor polarization value from the more easily measured vector polarization. Techniques to address this issue are only at the R&D stage at this time.
 - (b) As it is not clear how to measure the target tensor polarization obtained through “RF hole burning,” it is proposed to calibrate the target polarization using known values of T₂₀ at low Q². As the target must be depolarized and repolarized many times throughout the experiment, can this calibrated polarization be relied upon to be stable as high Q² measurements are made?
3. Fringe fields from the upstream SHMS magnets (particularly the HB) may couple significantly to the target magnet and vice versa. This coupling should be investigated with an eye on stability and crosstalk during quench events, etc. (For example, if the HB quenches, will the collapsing field couple to the target and take it down too?)
4. The proposal text states one of the dominant systematics is target field stability. The field coupling between the SHMS HB and the target field noted above may also impact the net holding field at the target as a function of both the SHMS momentum (field) setting, and spectrometer angle. The proposal comments on knowing the holding field to dB/B at the 100 ppm level.
 - (a) Adding magnetic shielding to isolate these fields is a non-trivial undertaking and may be difficult with the SHMS at small angles.
5. Will the effective target density change between polarized/unpolarized runs due to ND₃ bead displacement/resettling during the LHe boil-off/refill procedure used to kill the polarization? The text suggests this may result in a 10⁻³ change in eff. target length, but that such rearrangements would be immediately noticed as a change in the NMR signal. If such a disturbance is noted, can one then correct for it, or are the prior data unusable?
6. Tracking BCM and BPM drifts at < 100 nA beam currents over the long periods used for the polarized and unpolarized runs will be challenging. The proposal suggests adding temperature monitoring and recirculating heat regulation systems to the BCM pillbox and analog cabling.

- (a) Implementation and verification of such systems will require significant lead time and human resources.
- (b) It should be noted that 75 nA is the nominal “lower limit” of the existing readout systems in Hall C. New high gain electronics will be needed to reliably measure at lower beam currents.”

4.5 PAC42 Program Advisory Committee

“Measurement and Feasibility: Electron scattering off tensor-polarized deuterium would be measured in the quasi-elastic region using the Hall C HMS and SHMS spectrometers. This proposal would use the same setup as the C1-approved experiment E12-13-011, which is to measure the deuteron tensor structure function b_1 . The C1-approval is subject to demonstration that 35% tensor polarization is possible. The expected asymmetry is larger in the case of this measurement, but we anticipate that a similar requirement would apply. It is anticipated that a full proposal would be for 39 days, which would include 30 days for three different Q^2 values and 9.1 additional days of overhead.

Issues: A significant amount of beam time will be required for this measurement. A full proposal will need a detail discussion of expected systematic and statistical errors similar to what is in the letter that carefully justifies the requested time. The proposal should also demonstrate what sensitivity they will have to NN interaction models, such as the 6-quark model, final state interaction models, and NN interaction models, mentioned in the proposal. It will also be important to discuss how the results will distinguish between effects from the NN-interaction, the treatment of these interactions at high virtuality, and the intrinsic deuteron wave function.

Recommendation: Proceed to proposal addressing the issues noted above.”

4.6 PAC43 Program Advisory Committee

“Motivation: The motivation of the proposed experiment is to probe short-range repulsion and tensor force in nucleon-nucleon interaction by measuring tensor asymmetries from quasi-elastic and elastic deuteron scattering - tensor asymmetries are predicted to be sensitive to the D state probability in the deuteron wave function, as well as relativistic effects. The additional proposed measurement on T_{20} will also provide data for this observable.

Measurement and Feasibility: The proposed measurements will be carried out in Hall C using a tensor polarized deuteron target, the HMS, and the SHMS spectrometers. The proposed kinematic settings were chosen to cover both the quasi-elastic and elastic kinematics in order to provide data on T_{20} as well as calibration of the tensor polarization measurement using an existing data point from NIKHEF at low momentum transfer squared. The proposed measurements appear feasible and there are no

major technical issues with the assumption that a tensor polarization of 30% or more will be achieved before the proposed experiment will run.

Issues: The measurements, as proposed, will rely solely on positive tensor polarization due to the current UVa target setup. This has two drawbacks: (i) lower positive tensor polarization compared with the negative case; (ii) potential systematic issue associated with the ability to measure tensor asymmetries with only positive tensor polarization. The proponents are strongly encouraged to investigate techniques to obtain negative tensor polarization in addition to the positive tensor polarization. While the proposed measurements are important, the PAC believes more work is needed to demonstrate the impact of the measurements in the following two areas: (i) higher tensor polarization, particularly the negative one, should reduce uncertainties in the region that is sensitive to short-range repulsion and tensor force; (ii) provide quantitative comparison between the proposed tensor asymmetry and unpolarized measurements regarding sensitivity to the D-state probability. The NMR technique using line shape analysis for the tensor polarization determination needs to be further developed.

Recommendation: Conditional approval (C2).”

4.7 Response to PAC42 Concerns

The tensor polarization of 30% used in the rates for this proposal is the same as condition on the E12-13-011 proposal, which was incorrectly mentioned as 35%. Although DNP targets have been operated using beam energies up to 100 nA [75, 61], to ensure that the target polarization is not significantly affected by heating from the electron beam we’ve reduced our proposed current from 90 nA in the LOI to a more conservative 80 nA. We have expanded upon our estimated statistical and systematic uncertainties in Section 3.4 and in a recent technical note [60], where we stress that a measurement of A_{zz} in the quasi-elastic and $x > 1$ region is ideal for understanding time-dependent systematic effects without significantly affecting the measurement, as it is an order of magnitude less sensitive to drift effects than b_1 . Furthermore, we will be measuring T_{20} at low Q^2 where the observable is well understood both experimentally and theoretically, which can be used as a calibration and as a systematic check on the NMR measurement of the polarization. There has also been a dedicated effort made in understanding the tensor-enhanced polarization state by the UVA group over the past few years. Through studying tensor polarization enhancement and NMR line-shape analysis over multiple cool-downs, the UVA group is confident that the uncertainty in polarization can be kept to $< 6\%$ [53, 54]. However, even a very conservative estimate of 12%, as given in LOI12-14-002, would make for a compelling measurement.

Since PAC42, we have engaged a number of theorists who have provided calculations not only between light cone and virtual nucleon models, but also using different NN interaction potentials [7], and from on- and off-shell contributions to final state interactions (FSI) [37]. Deviations based on NN potentials and FSI only become apparent at large $x > 1.3$, so that the low $x < 1.3$ region can be used to discriminate between light cone and virtual nucleon calculations. Furthermore, A_{zz} calculations based on NN potentials are currently being systematically studied at low Q^2 by W. Van Orden and are expected to be completed within a year [8]. Although not completed

at the time of this proposal, G. A. Miller is still engaged in providing calculations of 6 quark effects in the elastic region [41]. Additionally, the proposed A_{zz} measurements are also ideal for making simultaneous high-precision measurements of T_{20} to test existing calculations up to large Q^2 , as discussed in Section 3.2, including in the region where Hall C and MIT-Bates data show a discrepancy, which requires only four more days of beam time than initially proposed in the LOI. Along with the ground-breaking measurements of A_{zz} in the $x > 1$ region, we will also be measuring T_{20} in the largest Q^2 range ever taken in a single experiment.

4.8 Response to PAC43 Concerns

Significant progress has been made in the past year both within motivating new theoretical developments that show the importance of tensor polarization compared to the vector polarized or unpolarized cases, as well as continued R&D efforts which have seen a $> 30\%$ tensor polarization enhancement on deuterated butanol.

Calculations provided by H. Arenhovel of all $D(e, e')$ observables at each of our kinematics are presented in detail in Sec. 1.1.1, which quantified that tensor polarized observables are the only current experimental method that is largely sensitive to the hardness or softness of the deuteron wavefunction, which is directly related to the sensitivity of the D-state probability. The difference in sensitivity between the tensor asymmetry A_{zz} and other methods is greater than a factor of 40.

Within the past months, the UVA target group has been advancing tensor polarization and has recently achieved $> 30\%$ tensor polarization on deuterated butanol in the lab, and is currently in progress of transferring these techniques to ND_3 , as described in Sec. 3.5.3. Additionally, there has been a dedicated effort to fully understanding the tensor polarization from line-shape analysis, with a publication on the most recent UVA results currently in review in Eur.J.Phys. A. Although we fully expect to be able to use this NMR line-shape method to measure polarization, at the time of running this technique will be directly compared to a completely independent tensor polarization extraction from the T_{20} observable. By making this cross-comparison at any Q^2 , we can remove any doubt that the line-shape polarization method is valid.

The PAC43 Technical Advisory Committee also raised concerns about fringe fields from the SHMS. These fields will play a negligible role in holding field as described in Sec. 3.5.6, where it is expected that we will be able to maintain dB/B at the 100 ppm or better level. Additionally, we don't expect coupling of the fringe fields to cause any negative effects in the case of a quench, particularly as the same target system did not see any ill effects during similar events when the g2p experiment ran in Hall A.

The final comment from the PAC43 Technical Advisory Committee directly relates to the two remaining issues from the PAC in regards to using only positive tensor polarization. Unfortunately, with the current method of tensor enhancement using a 1 K refrigerator in the DNP target we will be unable to maintain a negative tensor polarization while the beam is on the target, as discussed in Sec. 3.5.3. To mitigate any systematic effects caused by this concern, we plan to take very careful consideration of all time-dependent systematics as laid out in Sec. 3.4.2 and [60]. As noted, this will involve a significant lead time, but this process will lead to better systematics for the entire Jefferson Lab tensor program, as well as any future experiments within Hall C. Additionally, since we can create a positive tensor polarization and enhancement from either a positive or negative

initial vector polarization, we plan on flipping the vector polarization at each target repolarization to further eliminate systematics, as discussed in Sec. 3.5.4.

Although this experiment will be challenging, we note that all previous PACs have encouraged further development of this proposal. We are encouraged by the comment made by PAC43, “The proposed measurements appear feasible and there are no major technical issues with the assumption that a tensor polarization of 30% or more will be achieved before the proposed experiment will run.” The authors listed on this proposal reflect the available expertise in both theoretical and experimental techniques that will allow us to further explore the nature of pn correlations in nuclei, the discovery of which has been one of the most important results of the JLab 6 GeV program.

5 Summary

We propose to make a high precision measurements of the tensor asymmetry A_{zz} covering the kinematic range from the quasi-elastic ($x \approx 1$) up to elastic scattering ($x = 2$) that will provide valuable new insights about the high momentum components of the deuteron wavefunction. By incorporating both a tensor polarized target and the choice of $x > 1$ kinematics, A_{zz} amplifies short-range effects. Several theorists have provided state-of-the-art calculations of light cone, virtual nucleon, and final state interactions at various NN potentials, which have shown that A_{zz} is sensitive to both relativistic effects starting at $x < 1.4$ at $> 6\sigma$, and is sensitive to hard and soft NN potentials at $x > 1.4$ at up to $> 4\sigma$. This is the same kinematic region that has been shown to be correlated with the EMC effect via the $x > 1$ A/D (e, e') results. As described by the PAC42 and PAC43 theory reviews, a measurement of A_{zz} would “further explore the nature of short-range pn correlations in nuclei, the discovery of which has been one of the most important results of the JLab 6 GeV nuclear program.”

This measurement of A_{zz} also allows for a simultaneous measurement of the tensor analyzing power T_{20} without any further beam time or equipment by making a kinematic cut on the elastic peak. The lowest Q^2 measurement will fall on the most experimentally probed and theoretically understood region, making it ideal for calibrating the tensor polarized target. This measurement will also provide high-precision T_{20} data at $Q^2 \approx 0.7(\text{GeV}/c)^2$, where previous JLab data systematically disagrees with results from MIT-Bates. We will also measure T_{20} to the largest Q^2 value ever taken, providing a crucial test of the only existing data at $Q^2 > 1$. These T_{20} measurements will cover the largest range in Q^2 ever measured by a single experiment.

With 34 days of beam and an additional 11 days of overhead, A_{zz} can be measured with high precision at $Q^2 = 0.2, 0.3, 0.7, 1.5, 1.8$ and $2.9 (\text{GeV}/c)^2$ and T_{20} at $Q^2 = 0.3, 0.7, 1.5,$ and $1.8 (\text{GeV}/c)^2$ in Hall C using identical equipment as the upcoming b_1 measurement while being orders of magnitude less sensitive to systematic uncertainties and measuring asymmetries of order 100%. In addition, this data will fill a gap in measurements of A_{zz} between the $T_{20} \propto A_{zz}$ elastic measurements and the $b_1 \propto \frac{A_{zz}}{F_1^d}$ deep-inelastic measurements. This experiment will play a crucial role in the larger tensor program at Jefferson Lab, which continues to generate interest from experimental, polarized target, and theoretical spin communities, by providing the first experimental data in an region where there remains a gap in our understanding of the simplest composite nuclear system.

References

- [1] A. K. A. Azzam *et al.*, *Chin.J.Phys.* **43**, 813 (2005).
- [2] J. L. Forest *et al.*, *Phys. Rev.* **C54**, 646 (1996).
- [3] J. Arrington, D. Higinbotham, G. Rosner, and M. Sargsian, *Prog.Part.Nucl.Phys.* **67**, 898 (2012).
- [4] I. Korover *et al.*, *Phys.Rev.Lett.* **113**, 022501 (2014).
- [5] R. Schiavilla, R. B. Wiringa, S. C. Pieper, and J. Carlson, *Phys.Rev.Lett.* **98**, 132501 (2007).
- [6] L. Frankfurt and M. Strikman, *Phys.Rept.* **160**, 235 (1988).
- [7] M. M. Sargsian and M. I. Strikman, *J.Phys.Conf.Ser.* **543**, 012009 (2014).
- [8] W. Van Orden, private communication.
- [9] I. Passchier, L. van Buuren, D. Szczerba, R. Alarcon, T. Bauer, *et al.*, *Phys.Rev.Lett.* **88**, 102302 (2002).
- [10] W. P. Ford, S. Jeschonnek, and J. Van Orden, *Phys.Rev.* **C90**, 064006 (2014).
- [11] L. L. Frankfurt and M. I. Strikman, *Phys. Rept.* **76**, 215 (1981).
- [12] L. Frankfurt, M. Strikman, D. Day, and M. Sargsian, *Phys.Rev.* **C48**, 2451 (1993).
- [13] J. Arrington, C. Armstrong, T. Averett, O. K. Baker, L. de Bever, *et al.*, *Phys.Rev.Lett.* **82**, 2056 (1999).
- [14] N. Fomin, J. Arrington, R. Asaturyan, F. Benmokhtar, W. Boeglin, *et al.*, *Phys.Rev.Lett.* **108**, 092502 (2012).
- [15] W. Boeglin *et al.*, *Phys.Rev.Lett.* **107**, 262501 (2011).
- [16] W. Boeglin and M. Sargsian, *Int.J.Mod.Phys.* **E24**, 1530003 (2015).
- [17] M. Garcon and J. Van Orden, *Adv.Nucl.Phys.* **26**, 293 (2001).
- [18] S. Veerasamy and W. N. Polyzou, *Phys. Rev. C* **84**, 034003 (2011).
- [19] R. Machleidt, K. Holinde, and C. Elster, *Phys. Rept.* **149**, 1 (1987).
- [20] R. Machleidt, *Phys. Rev.* **C63**, 024001 (2001).
- [21] W. Leidemann, E. Tomusiak, and H. Arenhovel, *Phys.Rev.* **C43**, 1022 (1991).
- [22] I. Passchier *et al.*, *Phys. Rev. Lett.* **82**, 4988 (1999).

- [23] H. Zhu, Ph. D Thesis. (2000).
- [24] L. Weinstein, E. Piasetzky, D. Higinbotham, J. Gomez, O. Hen, *et al.*, Phys.Rev.Lett. **106**, 052301 (2011).
- [25] F. Gross, Phys.Rev. **C26**, 2203 (1982).
- [26] W. Buck and F. Gross, Phys.Rev. **D20**, 2361 (1979).
- [27] L. Frankfurt and M. Strikman, Nucl.Phys. **B148**, 107 (1979).
- [28] J. D. Terry and G. A. Miller, (2016).
- [29] L. Alexa *et al.*, Phys.Rev.Lett. **82**, 1374 (1999).
- [30] J. Van Orden, N. Devine, and F. Gross, Phys.Rev.Lett. **75**, 4369 (1995).
- [31] S. Rock, R. G. Arnold, P. E. Bosted, B. T. Chertok, B. A. Mecking, I. A. Schmidt, Z. M. Szalata, R. York, and R. Zdarko, Phys. Rev. **D46**, 24 (1992).
- [32] M. Sargsian, private communication.
- [33] M. M. Sargsian, Phys.Rev. **C82**, 014612 (2010).
- [34] F. Gross and A. Stadler, Phys.Rev. **C82**, 034004 (2010).
- [35] G. A. Miller and B. C. Tiburzi, Phys.Rev. **C81**, 035201 (2010).
- [36] W. Cosyn and M. Sargsian, J.Phys.Conf.Ser. **543**, 012006 (2014).
- [37] W. Cosyn, private communication.
- [38] W. Cosyn, W. Melnitchouk, and M. Sargsian, Phys.Rev. **C89**, 014612 (2014).
- [39] M. Strikman, private communication.
- [40] H. Arenhovel, private communication.
- [41] G. Miller, private communication.
- [42] S. Liuti, private communication.
- [43] R. Holt and R. Gilman, Rept.Prog.Phys. **75**, 086301 (2012).
- [44] R. A. Gilman and F. Gross, J.Phys. **G28**, R37 (2002).
- [45] D. Abbott *et al.*, Phys.Rev.Lett. **84**, 5053 (2000).
- [46] M. Bouwhuis, Z. Zhou, M. Ferro-Luzzi, E. Passchier, R. Alarcon, *et al.*, Phys.Rev.Lett. **82**, 687 (1999).
- [47] K. Slifer, *et al.*, Jefferson Lab PAC40 Proposal, E12-13-011 (2014).

- [48] T. Donnelly and A. Raskin, *Annals Phys.* **169**, 247 (1986).
- [49] M. H. Moore, B. P. Waidyawansa, S. Covrig, R. Carlinin, and J. Benesch, *JINST* **9**, T11002 (2014).
- [50] P. Bosted and V. Mamyan, e-print **arXiv:1203.2262**, (2012).
- [51] E. Long *et al.*, JLab Technical note, JLAB-TN-13-029 (2013).
- [52] D. Keller, *Nucl. Instrum. Meth.* **A728**, 133 (2013).
- [53] D. Keller, PoS **PSTP2013**, 010 (2013).
- [54] D. Keller, *Int.J.Mod.Phys.Conf.Ser.*, The 21st International Symposium on Spin Physics (2014), in press.
- [55] C. D. Keith *et al.*, *Nucl. Instrum. Meth.* **A501**, 327 (2003).
- [56] C. Yan, JLab Hall C Technical Note,
http://hallcweb.jlab.org/document/howtos/slow_raster.pdf.
- [57] W. A. Tobias, PhD. Thesis. (2001).
- [58] Russell J. Donnelly, <http://pages.uoregon.edu/rjd/vapor2.htm>.
- [59] A. W. Hewat and C. Riekel, *Acta Crystallographica Section A* **35**, 569 (1979).
- [60] D. Keller, JLab Technical note, JLAB-TN-15-014 (2015).
- [61] J. Pierce, J. Maxwell, T. Badman, J. Brock, C. Carlin, *et al.*, *Nucl.Instrum.Meth.* **A738**, 54 (2014).
- [62] W. Meyer *et al.*, *Nucl. Instrum. Meth.* **A244**, 574 (1986).
- [63] C. Dulya *et al.*, *Nucl. Instrum. Meth.* **A398**, 109 (1997).
- [64] Z. Zhou, M. Ferro-Luzzi, J. van den Brand, H. Bulten, R. Alarcon, *et al.*, *Nucl.Instrum.Meth.* **A378**, 40 (1996).
- [65] M. Bouwhuis, R. Alarcon, T. Botto, J. van den Brand, H. Bulten, *et al.*, *Phys.Rev.Lett.* **82**, 3755 (1999).
- [66] D. Keller, PoS **PSTP2013**, 010 (2013).
- [67] D. Keller, *J. Phys. Conf. Ser.* **543**, 012015 (2014).
- [68] D. Keller, *Int. J. Mod. Phys. Conf. Ser.* **40**, 1660105 (2016).
- [69] D. Keller, PoS **PSTP2015**, 014 (2016).
- [70] D. Keller, *Eur.J.Phys. A* (2016), under review.

- [71] S. Bueltmann, D. Crabb, Y. Prok. *UVa Target Studies*, UVa Target Lab technical note, 1999.
- [72] S. L. Bueltmann *et al.*, Nucl. Instrum. Meth. **A425**, 23 (1999).
- [73] O. Rondon-Aramayo, J.Phys.Conf.Ser. **543**, 012013 (2014).
- [74] K. Slifer, private communication.
- [75] T. D. Averett *et al.*, Nucl. Instrum. Meth. **A427**, 440 (1999).